Nanosized Authigenic Magnetite and Hematite Particles in Mature‐Paleosol Phyllosilicates: New Evidence for a Magnetic Enhancement Mechanism in Loess Sequences of China

Hyodo, Masayuki ; Sano, Takuroh ; Matsumoto, Megumi ; Seto, Yusuke ; Bradák, Balázs ; Suzuki, Kota ; Fukuda, Jun‐ichi ; Shi, Meinan ; Yang…

(Citation)
Journal of Geophysical Research. Solid Earth,125(3):e2019JB018705-e2019JB018705

(Issue Date)
2020-03-05

(Resource Type)
journal article

(Version)
Accepted Manuscript

Nano-sized authigenic magnetite and hematite particles in mature-paleosol phyllosilicates: New evidence for a magnetic enhancement mechanism in loess sequences of China

*Masayuki Hyodo[1,2], Takuroh Sano[2], Megumi Matsumoto[3,4], Yusuke Seto[2], Balázs Bradák[1,5], Kota Suzuki[2], Jun-ichi Fukuda[1], Meinan Shi[6], Tianshui Yang[7]

[1] Research Center for Inland Seas, Kobe University, Kobe 657-8501, Japan

[2] Department of Planetology, Kobe University, Kobe 657-8501, Japan

[3] Center for Supports to Research and Education Activities, Kobe University, Kobe 657-8501, Japan

[4] Department of Earth and Planetary Materials Science, Tohoku University, Sendai 980-8578, Japan

[5] Department of Physics, Escuela Politécnica Superior, University of Burgos, 09006 Burgos, Spain

[6] School of Ocean Sciences, China University of Geosciences, Beijing 100083, China

[7] School of Earth Sciences and Resources, China University of Geosciences, Beijing 100083, China

* Corresponding author: Masayuki Hyodo (mhyodo@kobe-u.ac.jp)

Key points:

- Hundreds of nanometer–micron-sized authigenic magnetite/hematite particles are concentrated in paleosol muscovite/chlorite grains.
- The authigenic iron-oxides are mainly responsible for the weak spontaneous magnetization of weathered muscovite and chlorite grains.
- Elongated authigenic magnetites account for the dominant single domain/vortex state magnetic property and magnetic enhancement in paleosols.

Key words:

pedogenic magnetic mineral, vortex state, TEM/SEM, synchrotron radiation XRD, muscovite, chlorite

Abstract

Magnetic enhancement of Chinese loess–paleosol sequences has been used extensively as a proxy for East Asian summer monsoon variations. However, the pedogenic magnetic particles contributing to this magnetic enhancement are difficult to extract, so it is not clear how they formed. In this study, we reveal pedogenic magnetite and hematite using electron microscopy, synchrotron radiation X-ray diffraction, and rock magnetic methods. First-order reversal curves indicate that superparamagnetic/single domain/vortex state magnetic properties dominated both loess and paleosol samples. Samples of muscovite and chlorite, which are paramagnetic, have weak spontaneous magnetization. The 1–10-μm-size fraction of host silicates is responsible for most of the magnetic enhancement of paleosols. In the paleosol fraction, we found weathered phyllosilicates (muscovite/chlorite), including many elongated submicron-to-a few microns authigenic magnetite and hematite particles between layers; however, few such interlayer particles were found in phyllosilicates of the loess fraction. The concentration of magnetite/hematite particles within paleosol muscovite/chlorite grains and in aggregates of phyllosilicate fragments is much higher than that of the submicron iron-oxides found on silicate surfaces. Interlayer magnetite particles are dominantly prism-shaped with aspect ratios > ~ 4. The authigenic magnetite must be mainly responsible for the spontaneous magnetization of the muscovites and chlorites and the paleosol magnetic properties. The protective silicates account for the low extraction efficiency and also the near-absence of surface oxidation of pedogenic magnetite. Based on our results, we suggest that magnetite/hematite in weathered phyllosilicates contribute significantly to the magnetic enhancement of mature paleosols.

1. Introduction

Loess–paleosol sequences across the Chinese Loess Plateau (CLP) provide an important archive of Pleistocene terrestrial climate changes (Heller and Evans, 1995; Liu *et al*., 2007; Maher, 2016). Magnetic enhancement of Chinese paleosols has been used extensively as a proxy for East Asian summer monsoon variations (e.g., Maher *et al.*, 1994; Maher and Thompson, 1995; Balsam *et al*., 2011). The magnetic susceptibility of this loess is low, and is significantly higher in paleosols. Enhancement in magnetic susceptibility of each paleosol layer is reflected by variations in the quantities of fine-grained pedogenic ferrimagnets whose formation depends on the strength of summer monsoon precipitation (Zhou *et al*., 1990; Maher and Thompson, 1991; Verosub *et al*., 1993; Liu *et al*., 2004).

Magnetic susceptibility enhancement in a paleosol is mainly attributable to superfine (< 100 nm) ferrimagnets consisting of superparamagnetic (SP) and single-domain (SD) particles (Maher and Thompson, 1991; Evans and Heller, 1994; Liu *et al*., 2007). Nevertheless, in contrast, magnetic hysteresis parameters of loess/paleosol samples of different ages from various sites across the CLP have been argued to be coarser because almost all data fall within the pseudo-single-domain (PSD) region on Day plots (Yang *et al*., 2008; Jin and Liu, 2010, 2011; Guo *et al*., 2002). The predominant interpretation of PSD magnetic properties within paleosol samples is inconsistent with the consensus that SP/SD pedogenic ferrimagnets contribute strongly to magnetic enhancement. This contradiction has never been addressed. Some studies have demonstrated that particles of approximately 0.1–10 μm size may contribute to magnetic enhancement (Sun *et al*., 1995; Liu *et al*., 2003, 2004). Such pedogenic magnetic particles have hardly been extracted from paleosols in China.

The procedures used to investigate pedogenic magnetic particles include rock magnetic studies of bulk/fractional sediments (Han and Jiang, 1999; Spassov *et al*., 2003), analysis of magnetic mineral extracts (Maher and Thompson, 1992; Liu *et al*., 2003, 2004), and analysis of residues of chemical separations after removal of citrate–bicarbonate–dithionite (CBD)-soluble fine magnetic grains (Verosub *et al*., 1993; Sun *et al*., 1995; van Oorschot and Dekkers, 1999). It is difficult to extract pedogenic magnetic particles, so little is known about their shape and size. For example, Liu *et al*. (2004) obtained magnetic extracts from loess and paleosol samples using a continuous loop flow driven by a pump and a high-gradient magnet. The extraction efficiency measured as magnetic susceptibility was approximately 70% for loess and < 20% for paleosol samples. The relatively high extraction efficiency for loess samples suggests that magnetic particles in these sediments consist predominantly of highly extractable, coarse detrital magnetic particles. In contrast, the low extraction efficiency for paleosol samples suggests that fine-grained pedogenic particles have been collected rarely. Therefore, magnetic extracts from paleosol samples are likely to be strongly biased toward detrital particles. Consequently, investigations using magnetic extracts from paleosol samples must be performed with caution.

In this study, we used loess and paleosol samples from two different regions of the CLP to seek to identify pedogenic magnetic particles responsible for magnetic enhancement. Our main target was coarser magnetic particles, which should be easier to detect than superfine particles. We used scanning electron microscope (SEM) and transmission electron microscope (TEM) observations, and synchrotron radiation X-ray diffraction (SR-XRD), in addition to rock magnetic experiments. We did not depend strongly on magnetic extraction techniques for sample separation. Instead, we separated samples according to grain size using gravitational settling and centrifugation (Han and Jian, 1999).

2. Materials and Methods

2.1 Samples

Sediments on the CLP consist of eolian dust that has been transported from deserts in the north–northwest by the winter monsoon (Kukla, 1987; Ding *et al*., 2000). Paleosols were formed in-situ by high summer precipitation during warm, moist interglacial periods, whereas loess sediments were deposited during cold, dry glacial periods with low levels of summer precipitation (Porter and An, 1995; Maher, 2016).

We used three pairs of samples collected at minimal and maximal magnetic susceptibility horizons in adjacent loess and paleosol units. The sampling sites are at Lingtai and Xifeng (approximately 100 km north of Lingtai) in the central CLP (Fig. S1). High-resolution magnetic susceptibility data have been obtained from these locations (Yang *et al*., 2010; Mishima *et al*., 2015; Ueno *et al.*, 2019). Samples were collected from loess L8 and the underlying paleosol S8 layers at both sites, and from paleosol S32 and the underlying loess L33 layers at Lingtai. The magnetic polarity stratigraphy in these regions (Liu *et al*., 1988; Sun *et al*., 2006) indicates that the L8–S8 and S32–L33 layers are approximately 0.78 and 2.6 Ma old, respectively. Samples from Lingtai are named LL8 for L8, LS8 for S8, LS32 for S32, and LL33 for L33. Samples from Xifeng are named XL8 for L8 and XS8 for S8. Each bulk sample was divided into three size fractions: > 10 μm (D1), 1–10 μm (D2), and < 1 μm (D3). We prepared four kinds of samples: bulk, D1, D2, and D3. We also prepared magnetic extract samples from the D2 fractions, which contribute dominantly to the magnetic enhancement.

2.2 Separation into grain-size fractions

We prepared a 2-g sample cube cut from a block sample and measured its magnetic susceptibility, weight, and volume. Powdered sediments (2 g) were then suspended in 1,000 mL of pure water that was ultra-sonicated in a beaker. The suspension was filtered through a 10-μm mesh filter, using a pipette to prevent clogging. Filtered D1 grains (> 10 μm) were transferred into a polycarbonate tube with pure water, centrifuged, and air dried. We transferred the filtered suspension into a polycarbonate tube and separated the precipitated 1–10-μm grains (D2) from the supernatant containing < 1-μm grains by centrifugation, in

accordance with Stokes' law. The supernatant was transferred into another polycarbonate tube and centrifuged more strongly until it was almost transparent. Finally, the supernatant was evaporated using hot, but not boiling, water. The final residue included the < 1-μm sample fraction (D3).

The magnetic susceptibility and mass of each fraction were measured in a polycarbonate tube. We estimated the loss of grains during treatment from magnetic susceptibility values and the masses of the bulk and size-fraction samples.

We also made magnetic extracts from the LL8 and LS8 D2 fractions, which we considered representative of loess and paleosol samples, respectively. These were used for electron microscopy. Distilled water was added to the dry sediments in polycarbonate tubes, and suspensions were obtained by ultra-sonication. A neodymium finger magnet in a glass tube was soaked in the suspension for 24 h, and the grains attracted by the magnet were rinsed off the glass tube. We collected the magnetic extracts and repeated this procedure for several days. The efficiency of this magnetic extraction procedure in terms of magnetic susceptibility was < 13% for both the LL8 and LS8 fractions.

2.3 Rock magnetic experiments

Rock magnetic analyses were performed as part of a preliminarily study of the pedogenic ferrimagnets and to identify the fractions most associated with magnetic enhancement. Low-field magnetic susceptibility (χ) and frequency-dependence of magnetic susceptibility (χ_{FD}) were measured using a SM-100 magnetic susceptibility meter (ZH Instrument Company, Brno, Czech Republic). We measured susceptibility three times for each specimen by selecting frequencies of 500 Hz ($\chi_{500\ Hz}$) and 16,000 Hz and calculated mean values. χ_{FD} was calculated using the formula $\chi_{FD} = \chi_{500\ Hz} - \chi_{16k\ Hz}$ can be used to estimate the content of viscous SP grains at approximately the SD–SP boundary (Liu *et al*., 2005).

Thermomagnetic analyses conducted in an air atmosphere were performed on bulk samples using an NMB-89 magnetic balance (Natsuhara Giken Corporation, Osaka, Japan). A sample was heated from 50°C to 700°C and cooled to 50°C at a rate of 10°C/min. Isothermal remanent magnetization (IRM) acquisition and hysteresis experiments were performed using a VSM MicroMag 3900 (Princeton Measurements Corporation). The IRM was measured at 100 steps from 0.1 to 1000 mT, and the data were analyzed using IRMUNMIX 2.2 software (Heslop *et al*., 2002). Magnetic domains were estimated using first-order reversal curve (FORC) measurements (Pike *et al.*, 1999; Roberts *et al.*, 2000) for another set of three pairs of bulk loess and paleosol samples collected near the horizons of the first set using a VSM MicroMag 3900. FORC distributions were processed using the FORCinel 1.18 software (Harrison and Feinberg, 2008) with smoothing factors of 3–5.

2.4 SR-XRD analysis

We performed SR-XRD experiments for bulk samples and for the D1, D2, D3, and D2 magnetic extracts of the LL8 and LS8 fractions using the AR-NE1 beam line at the synchrotron radiation facility Photon Factory in KEK, Tsukuba City, Japan. The SR-XRD technique can determine crystalline phases and their fraction volumes in a micro-volume sample by irradiating a finely converged X-ray beam. The incident X-ray beam used to irradiate the samples was monochromatized to a wavelength of 0.4185 Å and collimated to approximately 100 μm. The exposure time was 300 s for each measurement. Two-dimensional Debye ring patterns were recorded on a flat imaging plate and converted to 2θ-intensity profiles using the IPAnalyzer software (Seto *et al*., 2010). The 2θ-intensity profiles were then analyzed using the PDIndexer software (Seto *et al*., 2010) for crystalline phase identification. To estimate the volume of the phases, a Rietveld refinement was performed for each 2θ-intensity profile using GSAS-II software (Toby and Von Dreele, 2013). We used crystal structure data from quartz (Lignie *et al*., 2012), muscovite (Gatineau, 1963), chlorite (Zheng and Bailey, 1989), albite (Ribbe *et al*., 1969), hematite (Blake *et al*., 1966), and magnetite (Fleet, 1986) as input sources. The compositions of these minerals were adjusted to those of our samples by changing the site occupancies of atoms. The atomic positions in the unit cell were fixed during these refinements. The signals for magnetite and maghemite were mostly indistinguishable in XRD patterns because of their similar crystal structures, so the estimated magnetite content includes the maghemite content.

2.5 SEM and TEM observations

SEM observations were performed on thin sections of bulk D2 fractions and magnetic extracts of the LL8 and LS8 fractions using a JSM-6840LAII system (JEOL, Tokyo) equipped with an energy dispersive X-ray spectrometer (EDS), operated at 15 kV with a beam current of 0.4 nA. For the TEM observations, thin (50–100 nm) sections of the magnetic extracts solidified in resin were prepared using a focused ion beam system (Quanta 200 3DS, Thermo Fisher Scientific) at Kyoto University, Japan. Microstructure observations were recorded, and chemical analyses were performed on the D2 magnetic extracts of the LL8 and LS8 samples using a JEM-2100F scanning TEM (JEOL) equipped with a field emission cathode and an EDS system. Crystalline phases were analyzed based on selected-area electron diffraction using Gatan Digital Micrograph and ReciPro software (http://pmsl.planet.sci.kobe-u.ac.jp/~seto/).

3. Results

3.1 Separation into grain-size fractions

The loss of sample materials during the process of separation into fractions was only 0.5–3.5% in terms of mass, but it was 4.7–50.8% in terms of volume magnetic susceptibility (Table 1). The lost material includes fine-grained magnetic particles. Relatively small losses

for paleosol samples (< 18.1%), which were the main target of this study, suggest that our observations of magnetic particles in the D1, D2, and D3 fractions (> 80% in terms of volume magnetic susceptibility) are likely to be representative of a paleosol sample.

3.2 Magnetic susceptibility and frequency dependence of magnetic susceptibility

χ values for the bulk paleosol LS8, XS8, and LS32 samples were 115, 116, and 177 × 10^{-8} m^3 kg^{-1}, respectively, which were 4.0-, 6.3-, and 5.5-fold greater than those of the adjacent loess samples LL8, XL8, and LL33, respectively (Table 1). Therefore, all paleosol samples underwent strong magnetic enhancement. The size fractionated paleosol samples also have strong magnetic enhancement with χ values of 48–70 × 10^{-8} m^3 kg^{-1} for D1 (> 10 μm), 130–202 × 10^{-8} m^3 kg^{-1} for D2 (1–10 μm), and 228–338 × 10^{-8} m^3 kg^{-1} for D3 (< 1 μm) (Table 1). Therefore, finer grain-size fractions have higher χ values, which suggests that the concentration of pedogenic magnetic components in these fractions is higher. However, even the D1 and D2 paleosol fractions include pedogenic components because their χ values are much higher than 10–25 × 10^{-8} m^3 kg^{-1}, which is the estimated range for unweathered loess (Verosub *et al*., 1993; Vidic *et al*., 2000). Moreover, the D2 paleosol fraction contains a significant proportion of magnetically enhanced components (44–65% volume magnetic susceptibility for bulk sample) (Table 1). χ_{FD} data for the D2 paleosol fractions contribute significantly to the bulk χ_{FD}. Therefore, the D2 fractions were the main targets for identifying the pedogenic ferrimagnets responsible for magnetic enhancement.

Extremely high χ values of > 800 × 10^{-8} m^3 kg^{-1} that correspond to approximately 20–30-nm magnetite (Maher, 2016) are estimated for the lost LS8 and XS8 grains. The lost material probably contained highly condensed ultrafine ferrimagnets. Although it is generally accepted that these ultrafine ferrimagnets are mainly responsible for magnetic enhancement in paleosols (Zhou *et al*., 1990; Maher and Thompson, 1991; Verosub *et al*., 1993), the material lost in this study comprises < 18% of the bulk magnetic susceptibility.

χ values for the LL8, XL8, and LL33 loess samples are 28.9, 18.4, and 31.9 × 10^{-8} m^3 kg^{-1}, respectively. χ values for the LL8 and LL33 samples indicate that these loess samples had undergone weak magnetic enhancement. In these samples, as in paleosol samples, the D2 fractions make the greatest contribution to the bulk χ and χ_{FD}. In the CLP, loess layers rich in carbonate concretions have low susceptibility values of approximately 10 × 10^{-8} m^3 kg^{-1}, which reflects the diamagnetism of calcite and/or quartz (Maher, 2016). The XL8 sample was collected just below a 20-cm-thick calcareous concretion layer (Yang *et al*., 2010), and its χ values may have been affected by diamagnetic components. Therefore, even the XL8 sample could have been magnetically enhanced.

3.3 Thermomagnetic analysis

Heating curves from thermomagnetic experiments in an air for all loess and paleosol

samples indicate that the magnetization decreases at approximately 580°C and 680°C, which indicates the presence of magnetite and hematite, respectively (Fig. 1). In addition, the presence of maghemite is evident from inflections in the heating curves at 250–400°C and the absence of corresponding signals in cooling curves (Deng *et al.*, 2001). Maghemite decomposes thermally at 250–400°C and is then oxidized to form to hematite. The loess and paleosol sediments contain detrital lithogenic magnetite particles in the multi-domain (MD) to vortex state size range, with ultrathin maghemite shells that result from low-temperature oxidation around their rims (Cui *et al.*, 1994; van Velzen and Dekkers, 1999; Liu *et al*., 2003, 2004). Inflections in loess heating curves at 250–400°C are larger than those in paleosol heating curves, which suggests that the relative maghemite content in pedogenic ferrimagnets that dominate the paleosol samples is low. The thermomagnetic curves also undergo clear magnetization loss upon cooling, which partly reflects oxidation of strongly magnetic maghemite to form weakly magnetic hematite, and the oxidation of fine-grained magnetite. The reductions were 35–40% for loess samples and 20–30% for paleosol samples. The small reductions for paleosol samples suggest that the maghemite content was low and/or that fine-grained pedogenic magnetite was mostly not affected by high-temperature oxidation to form hematite. These topics are discussed along with IRM spectra in the next section.

3.4 IRM spectra

Three-component fitting provides the best fit model for the IRM acquisition spectra of all samples. The results indicate that the IRM components have gradient maxima of approximately 30, 80, and > 200 mT for $B_{1/2}$, for both loess and paleosol bulk samples (Fig. 2). The only difference between the loess and paleosol samples was their relative contributions (Table S1). Among the bulk samples, the low $B_{1/2}$ component (~30 mT) is predominant in paleosol samples, whereas the medium $B_{1/2}$ component (~80 mT) is dominant in loess samples, with the exception of LL33 (Table S1). The relative contributions of the components change in the different fractions. The low $B_{1/2}$ component is predominant in the D2 (1–10 μm) and D3 (< 1 μm) paleosol fractions. The medium $B_{1/2}$ component is dominant in the D1 and D2 loess and the D1 (> 10 μm) paleosol fractions, but it is absent from all D3 fractions. The high $B_{1/2}$ component (> 200 mT) is moderately represented in all fractions.

The remanent coercive force of intergrown SD–PSD magnetite ranges from approximately 20 to 50 mT (Heider *et al.*, 1996). Based on thermomagnetic analyses (Fig. 1), the low $B_{1/2}$ (~30 mT) component, which dominates in the medium/fine paleosol fractions, must be dominated by pedogenic magnetite. The high $B_{1/2}$ (> 200 mT) component, which is present in all loess/paleosol fractions with wide distributions (i.e., large dispersion parameter, DP), comprises detrital and pedogenic hematite. The medium $B_{1/2}$ (~80 mT) component dominates the coarse/medium loess fractions and the coarse paleosol fractions, but is absent from the fine fractions, which include coarse detrital magnetite with maghemite rims. The

maghemite rim increases the coercivity of a magnetite particle due to the enhanced stress induced by the oxidation gradient between the maghematized rim and the magnetite core (Cui *et al.*, 1994; van Velzen and Zijderveld, 1995). This stress is produced by different lattice constants of the maghemite rim and magnetite core. The higher $B_{1/2}$ values of the coarse detrital magnetite particles in this study are probably caused by this stress.

The loss of sample magnetization after heating and cooling treatments (Fig. 1a) correlates linearly with the medium $B_{1/2}$ component (Fig. 1b). Correlation lines for the loess and paleosol samples have similar gradients, which suggests that the thermal loss of magnetization is due mainly to coarse detrital magnetite with maghemite shells (i.e., maghemite decomposition), whereas pedogenic components hardly contribute to this process. Thus, most of the maghemite in the paleosol samples appears to be detrital, which is consistent with results of previous studies (Spassov *et al.*, 2003; Maher, 2016). The lines intercept the vertical axes (i.e., when coarse detrital magnetite is absent) at 11.9% for the paleosol and 20.4% for the loess samples. The intercept indicates that the loss of sample magnetization is due to high-temperature oxidation of fine-grained detrital/pedogenic magnetite in the low $B_{1/2}$ components (Table S1). Thus, the relative content of high-temperature-oxidized, fine-grained magnetite in paleosol samples is small, approximately half that in the loess samples. In summary, thermal loss of magnetization consists of two components—thermal decomposition of maghemite and high-temperature oxidation of fine-grained magnetite. Pedogenic magnetic particles contribute the least to both of these processes.

3.5 FORC diagrams

FORC diagrams for all loess and paleosol samples have the peak around 10 mT, which indicates a dominance of SD particles, with divergent distributions at low coercivities, which indicate the presence of MD or vortex state particles (Fig. 3). Loess samples in Figure 3a and 3b have higher coercivities, and broad vertical spread, which may be due to coarse detrital magnetite with maghemite shells (medium $B_{1/2}$ component in Fig. 2) (Roberts *et al.*, 2000). On the other hand, the lower coercivity and similar FORCs for all paleosol samples (Fig. 3d–f) imply that pedogenic magnetite dominates these samples (low $B_{1/2}$ component in Fig. 2). All FORC diagrams (Fig. 3) have asymmetrical diverging contours in the lower half plane close to the H_u axis due to SP particles (Roberts *et al.*, 2000; Pike *et al.*, 2001).

3.6 SR-XRD analysis

Clear peaks due to quartz, muscovite, chlorite, and albite, and faint signals due to magnetite/maghemite and hematite are observed in all XRD patterns (Fig. 4a), which is consistent with the typical major compositions of quartz, phyllosilicates, clay minerals, and iron-oxides in Chinese loess samples (Maher, 2016). Magnetite and maghemite have the same

spinel-type crystal structures and similar lattice constants. Therefore, these minerals have similar XRD patterns, except for the slight shift of maghemite peaks to higher angles than those of magnetite (Chen *et al*., 2010). Our samples probably include maghemite as thin rims surrounding coarse detrital magnetites. However, such signals are not isolated in our XRD data (Fig. 4a) due to the small amount of maghemite revealed by thermomagnetic and IRM component analyses.

Rietveld refinement results for the Lingtai D2 and D3 fraction samples are shown in Table 2. Reliable results with small residuals were unobtainable from the bulk and D1 samples, which include coarse grains. Both loess and paleosol samples comprise mainly quartz (43–48% by volume), muscovite (27–31%), chlorite (12–15%), and albite (11–13%), with small quantities of iron-oxides (approximately < 0.2%).

Magnetic mineral separation appears to have been effective, based on the sample compositions identified (Table 2). The hematite content of paleosol sample D2 LS8 increased from 0.2% in the bulk fraction to 0.8% in the extracts. The magnetite (/maghemite) content in paleosol D2 LS8 is nearly zero in the bulk fraction, but increased to 0.3% in the magnetic extract. In addition, magnetic separation clearly changed the sheet silicate content (Fig. 4b). To estimate mineral content changes in the extracts, we calculated the content of each mineral normalized to the quartz content of the bulk D2 loess and paleosol fractions compared to that in the D2 magnetic extracts. We assume that the quartz content does not change because of its strong resistance to weathering. The muscovite content normalized to the quartz content in the D2 fractions increased 3.3-fold in the loess and 4.9-fold in the paleosol (Fig. 4c). The chlorite content normalized to the quartz content in the D2 fractions increased 2.6-fold in the loess and 3.8-fold in the paleosol. These results suggest that paramagnetic chlorite and muscovite in both the loess and paleosol samples contain magnetic minerals that give rise to the measured magnetizations and that the magnetization intensities of paleosol muscovite/chlorite are higher than those of loess muscovite/chlorite. The latter should be caused by much larger amounts of pedogenic magnetic particles, especially large amounts of strongly magnetic magnetite. Thus, muscovite and chlorite may be hidden contributors to the magnetic enhancement of paleosols.

3.7 SEM images of silicates and iron-oxides

The D2 fractions of the LL8 loess and LS8 paleosol samples comprise similar silicate grains. However, these grains have slightly different shapes: loess grains are angular, whereas paleosol grains are more rounded due to weathering (Figs. 5a, S2). White arrows on the SEM images indicate small amounts of iron-oxides, at most a few microns in length (Fig. 5a). These iron-oxides are small compared to the characteristic X-ray excitation volume, so EDS iron-oxide spectra overlap with those of background silicates. Some of these iron-oxides may also occur within the muscovite (e.g., iron-oxide (2) in Fig. 5a and iron-oxide (1) in Fig. S2c).

These iron-oxide occurrences are similar to those observed in a paleosol sample from Xifeng (Yang *et al*., 2013). EDS data for iron-oxides (1) and (2) in Figure 5b and iron-oxide (1) in Figure S2c contain muscovite signals, which reflects signals due to intergrown or background silicates. Similar EDS data for the muscovite and chlorite grains, especially the presence of K in chlorite (Fig. 5b), suggest that the chlorite is a weathering product of the muscovite.

Comparing SEM images for the D2 fractions (Fig. 5a) indicates that there is no significant difference between the iron-oxide concentrations of loess and paleosol samples, although paleosol samples have a 4-fold higher magnetic susceptibility than loess samples (Table 1). Iron-oxide particles observed on silicate surfaces may not be a major contributor to the magnetic enhancement of paleosol fractions. However, their particle sizes, approximately 2 μm to several hundred nanometers, are consistent with vortex state sizes estimated based on FORCs (Figs. 3).

3.8 TEM images of iron-oxides

TEM analyses reveal large differences between loess and paleosol samples. The D2 LL8 loess magnetic extracts contain mainly less-weathered muscovite/chlorite and quartz grains, with small amounts of iron-oxide particles (Fig. 6a). There are a few aggregates with superfine (< 100 nm) Fe-bearing grains and silicate fragments. Aggregate (1) consists of fine-grained fragments with irregular shapes and sizes, whereas aggregate (2) contains elongated silicate fragments, some of which must be phyllosilicate fragments (Fig. 6a). The lower part of muscovite (1) is partly weathered and contains superfine-grained iron-oxides, and muscovite (2) contains a chlorite grain, which indicates a middle stage of forming chlorite from muscovite. Thus, this loess fraction has evidence of weak weathering. The aggregates contain 1–2-μm hematite grains and thin, elongated Fe-bearing materials, such as in the paleosol fraction mentioned below. The Fe-bearing materials may be pedogenic and contribute to the weak magnetic enhancement of the loess fractions. Inside the loess muscovite/chlorite grains, there is no iron-oxide particle, although they have superfine particles on their surfaces (Figs. 6a, 7a). Discrete hematite and magnetite particles, with sizes of hundreds of nanometers, which are probably detrital, are interspersed among the silicates (Fig. 8a, b).

In contrast to the loess fraction, the D2 LS8 paleosol magnetic extracts comprise many hundreds of nanometer-to-micron-sized iron-oxide particles within grains of muscovite and chlorite (Fig. 6b–d). The large chlorite grain at the top includes a few micron-sized elongated hematite particles between layers (hematite (1) and (2) in Fig. 6b). The aggregate that is spread widely in the lower part consists of a number of submicron-sized iron-oxide particles and elongated silicate particles, probably muscovite/chlorite fragments, aligned in parallel (Fig. 6b). The parallel alignments suggest that the aggregates comprise fragments of a weathered phyllosilicate. Small iron-oxide particles are highly condensed in the muscovite (1)

grain, whereas the muscovite (2) grain does not contain iron-oxide; however, nanometer-sized iron-oxide particles adhere to it or occupy its surface (Fig. 6b). It is noted that quartz grains are coated with fine-grained iron-oxide and silicate fragments. Within the large muscovite grain, elongated magnetite and hematite particles are distributed separately, and some particles form an aggregate with platy biotite (i.e., phyllosilicates) (Fig. 6c, d). These particles are several hundred nanometers long and a few to several tens of nanometers wide. Magnetite particles overlap on other particles within a 50–100 nm thick TEM section (e.g. Figs. 7c, 8e), which indicates that each magnetite particle is < 50–100 nm thick, and may be rectangular prism-like shaped. The dominant aspect (length/width) ratio for prism-like magnetite ranges from ~ 4 to > 10. Outside of the muscovite grain, iron-oxide plus biotite aggregate-like elongated particles surround the muscovite and chlorite fragments. Elongated Fe-bearing particles, a few micrometers in length and observed between muscovite fragment layers (Fig. 6c), seem similar to interlayer hematite grains in the chlorite (Fig. 6b) and the elongated Fe-bearing material in the loess sample (Fig. 6a). Authigenic hematite and magnetite particles are elongated (Fig. 8c−f), unlike those that are probably detrital (Fig. 8a, b). Paleosol chlorite and muscovite grains contain tens-of-nanometer iron-oxide particles between layers, but the total volume of these particles is much smaller than that of authigenic iron-oxide particles > 100 nm (Fig. 7b, 7c).

Elongated hematite particles included in the chlorite (Fig. 6b) just fit between layers, coming into tight contact with the upper layer (Fig. 9a). The lower boundary of the hematite particles is not sharp, and changes gradually to chlorite. The chlorite sheet structure below and to the left of the hematite is deformed. This may reflect weathering-related authigenic hematite formation within the chlorite. Weathering also probably deformed the phyllosilicate sheet structure of muscovite. Undulations are visible in layers of weathered paleosol muscovite fractions (Fig. 9b), in contrast to the parallel-layered structure visible in unweathered loess muscovite fractions (Fig. 9c). The sheet structure may have been deformed by authigenic Fe-bearing mineral formation, because undulations occur near these minerals. Iron-oxide inclusions occur between these undulating layers, with biotite layers parallel to muscovite layers. Although the ideal formula of muscovite is (KAl_2 [$AlSi_3O_{10}$] [OH F]$_2$), the mineral contains a small amount of Na and Ca, which replace K at the hexagonal prism site, and some Mg, Fe, and Mn, which replace Al at octahedral sites (Nishiyama, 1983). EDS data (Figs. 5b, S2d) indicate that muscovite and chlorite grains in both loess and paleosol samples contain small amounts of Fe. The Fe-bearing minerals biotite (K [Mg, Fe]$_3$ [$AlSi_3O_{10}$] [OH]$_2$), magnetite (Fe_3O_4), and hematite (Fe_2O_3) may have formed by water infiltration between layers that dissolved some of the muscovite to create ferric iron solutions. Considering another case of authigenic magnetic minerals (iron sulfides) formed within phyllosilicates (Roberts, 2015), iron-rich sheet silicates provide extensive reactive surfaces for interactions with pedogenic fluids under the required geochemical conditions to produce magnetite. A

model for transformation of ferrihydrite to hematite may hint partly at the formation process (Jiang *et al.*, 2018). The elongated hematite grains (Fig. 6b–d) may have been formed from capillary crystals of goethite (FeO [OH]) (Goss, 1987). Other inclusions of monazite ([Ce, La, Nd] PO_4) and anatase (TiO_2) could also have been formed by water (e.g., Halpin *et al.*, 2014; Morad, 1986).

4. Discussion

4.1 Origin of bulk SD, vortex state, and SP properties

FORC diagrams reveal that SD and vortex state (or MD) properties dominate all mature-paleosol samples (Fig. 3). In addition, magnetic enhancement is predominantly contributed by the D2 (1–10 μm) fractions (host silicates), which contain few MD (> 10–20 μm) particles. Therefore, pedogenic magnetite that is mainly responsible for magnetism in paleosols is found predominantly in SD and vortex state-sized particles. Authigenic magnetite particles that are a few to several hundreds of nanometers long, with aspect ratios > ~ 4, and that are included within weathered muscovite/chlorite and aggregates of phyllosilicate fragments (Fig. 6), are a prime candidate for these SD/vortex state particles. Particle shape exerts a critical control on domain state threshold sizes. According to calculations of domain state threshold sizes for magnetite particles with varying aspect ratios (Muxworthy and Williams, 2009), the stable SD to vortex state transition occurs at ~100 nm, 400–500 nm, and ~2 μm in length for particles with aspect ratios of about 1.5, 4, and 10, respectively. Therefore, prism-shaped authigenic magnetite particles found in this study are dominantly in the SD state, with vortex state particles, which is consistent with our interpretation of FORCs.

Ultrafine (< a few tens of nanometers) iron-oxide particles, the total volume of which is small, are concentrated between layers of chlorite grains, and on phyllosilicate surfaces (or in surface thin layers) (Figs. 6a, b, 7a, b). These particles should be the main contributor to the SP behavior observed in FORCs.

Based on the magnetic properties of magnetic extracts and corresponding loess and paleosol sample residues, Liu *et al*. (2004) proposed that fine-grained pedogenic PSD (i.e., vortex state) (~100 nm to several microns) particles contribute significantly to magnetic susceptibility enhancement in mature paleosol fractions with $\chi > (100–120) \times 10^{-8}$ m^3 kg^{-1}, whereas for paleosol fractions with moderate pedogenesis ($\chi < 100 \times 10^{-8}$ m^3 kg^{-1}) pedogenic SD particles are mainly responsible for magnetic susceptibility enhancement. Elongated authigenic magnetite particles in the hundreds-of-nanometer size range identified in this study provide evidence for the particles in mature paleosol fractions that Liu *et al*. (2004) proposed.

4.2 Contributors to magnetic enhancement

A high concentration of authigenic magnetite/hematite particles was found within weathered phyllosilicates (muscovite/chlorite) and aggregates of phyllosilicate fragments, and

phyllosilicates are abundant in paleosols. Thus, these authigenic magnetic particles should be the main pedogenic component and the major candidate for magnetic enhancement. Other candidates are discrete submicron iron-oxides on surfaces of chlorite and muscovite fragments (Fig. 6), and particles that are scattered among silicate grains (Fig. 5). Some of these are detrital, and some may be pedogenic iron-oxides. However, these discrete iron-oxides are minor compared to those included in phyllosilicates or aggregates (Figs. 5, 6).

The magnetic susceptibility of bulk paleosol sample LS8 was 4-fold greater than that of the bulk LL8 loess fraction (4.1-fold greater for D2 fractions) (Table 1). Magnetic enhancement is, therefore, mainly due to the increased pedogenic magnetite and hematite. The iron-oxide concentrations on silicate surfaces are similar between loess and paleosol samples (Fig. 5). By contrast, their concentrations on cross-sections of silicates are remarkably different— iron-oxides are much more concentrated in the paleosol (Fig. 6). To compare their concentrations in TEM images quantitatively, we estimated the proportion of the total Fe-bearing particle area relative to the total mineral area (FeM) using TEM elemental maps in Figure 6 (Fig. S3). FeM is 1.4% for the loess sample in Figure 6a, and 7.7% and 4.6% for paleosol samples in Figure 6b and 6c, respectively. Assuming that the FeM of a TEM image represents an average concentration of magnetite/hematite (plus small amounts of biotite) and that the volume content ratio of magnetite versus hematite is constant, the ratio of the paleosol FeM to the loess value (3.4−5.5-fold) should reflect magnetic enhancement. This ratio agrees roughly with the ratio of paleosol magnetic susceptibility to loess susceptibility (approximately 4-fold). Therefore, it is likely that authigenic magnetite/hematite particles are the main contributors to the magnetic enhancement of paleosols.

Submicron iron-oxide particles on silicate surfaces can be a candidate for fine-grained magnetites that are dissolved easily by CBD treatment (Verosub *et al.*, 1993; Sun *et al.*, 1995; van Oorschot and Dekkers, 1999) and contribute to magnetic enhancement. However, the total amount of these particles is likely insignificant. For example, the FeM estimated by the same method as above for quartz grains and Fe-bearing particles on silicate surfaces in Figure 6b was about 0.2% (Fig. S3), which is < 1/10 of the FeM for those particles within phyllosilicates and aggregates. Therefore, submicron authigenic magnetic particles in the weathered muscovite/chlorite grains and in aggregates of phyllosilicate fragments are the main contributor to magnetic enhancement. Interlayer magnetite particles in chlorite, a swelling clay mineral, are likely CBD-soluble, due to high water absorbency of chlorite. Negatively charged surfaces of swelling clay minerals attract positively charged water molecules, allowing the water to enter between layers and to cause the clay structure to expand. The water absorption occurs on picosecond time scales (Le Caër *et al.*, 2012). We consider weathered muscovite particles into which water infiltrated to cause interlayer magnetic mineral formation and/or partial chloritization as also likely to be hygroscopic, and thus superfine ferrimagnets within muscovite particles may be CBD-soluble.

4.3 Muscovite and chlorite grains contain minerals with spontaneous magnetization

Authigenic magnetite/hematite particles in phyllosilicates or aggregates of silicates found in this study can account for the following phenomena. (1) Muscovite and chlorite grains in the loess and paleosol samples are paramagnetic but must contain minerals with spontaneous magnetization, with much stronger intensities observed in paleosol samples (Fig. 4c). (2) This study and previous studies (e.g., Liu *et al*., 2003, 2004) have shown that the magnetic extraction efficiency of pedogenic magnetic particles is low, probably because magnetic particles are incorporated within heavy surrounding silicates (muscovite and chlorite). (3) Although superfine (< 100 nm) SD/SP ferrimagnets may be predominantly responsible for magnetic enhancement (Liu *et al*., 2007; Maher, 2016), in this study, the D2 (1–10 μm) fractions mainly comprising silicates are predominantly responsible for the magnetic susceptibility of paleosol fractions.

The magnetic extracts from both loess and paleosol samples contain fair amounts of silicates, including quartz (Fig. 4b). This indicates that the silicate grains probably contain magnetic inclusions of igneous origin (e.g., Chang *et al.*, 2016; Chen *et al.*, 2017), in addition to authigenic magnetic particles that formed within phyllosilicates in dust source (desert) areas before transportation as well as in the CLP after deposition.

4.4 Does pedogenic magnetite escape maghemitization?

Superfine (< 100 nm) SD and SP magnetite is easily oxidized completely into maghemite when exposed to air due to high surface area/volume ratios. In contrast, coarse detrital magnetite grains are partially oxidized at their surfaces, producing maghemite shells (Cui *et al.*, 1994; van Velzen and Zijderveld, 1995; van Velzen and Dekkers, 1999; Liu *et al*., 2004). However, our magnetic experiments suggest that maghemitization of superfine pedogenic magnetites occurs rarely or is negligible.

The loss of sample magnetization after heating and cooling treatments is less severe in paleosol samples compared to loess samples (Fig. 1). This reduction in magnetization loss in paleosol samples occurs despite these samples including large quantities of superfine pedogenic magnetite. This suggests that superfine magnetite in paleosol samples may have escaped high-temperature oxidation in air. This may be because most of these ferrimagnets are enclosed within phyllosilicate grains and fragments and are not directly exposed to air during thermal treatment. However, partial oxidation of authigenic magnetite particles during weathering will give rise to maghemitization in air, which may have been observed in magnetic extracts of loess/paleosol samples (e.g., Liu *et al*., 2003, 2004).

4.5 Timing of mineral authigenesis in phyllosilicates

The magnetic susceptibility of modern soils may provide a hint regarding the timing of

pedogenic ferrimagnet formation. Magnetic susceptibility reaches mature-paleosol values (> 100×10^{-8} kg^{-1}) at a near-surface layer (Yang *et al.*, 2015; Kang *et al.*, 2018), and have a linear relationship with proximal-site modern precipitation (Maher and Thompson, 1995; Balsam *et al.*, 2011). Thus, most pedogenic ferrimagnets form near the surface. In addition, centennial-scale anti-phase changes of magnetic susceptibility and eolian grain size (proxies of East Asian summer and winter monsoons, respectively) for the late Holocene (Kang *et al.*, 2018) and middle Pleistocene (Ueno *et al.*, 2019) suggest that pedogenic ferrimagnet formation was nearly syndepositional. Therefore, it is plausible that authigenic magnetic minerals formed within phyllosilicates shortly after dust deposition.

In loess, originally paramagnetic muscovite/chlorite particles (e.g., Borradaile and Werner, 1994; Martín-Hernández and Hirt, 2003) become magnetically enhanced so that they have a weak spontaneous magnetization (Fig. 4c). This may be evidence for weak post-depositional pedogenesis during glacial periods. Alternatively, they might have undergone weathering in their previous history because dust source regions must be products of weathering.

4.6 Strengthening of the initial fabric of loess

Anisotropy of magnetic susceptibility parameters for both loess and paleosol samples usually have fabrics dominated by lineation or foliation with a nearly horizontal principal magnetic susceptibility axis (e.g., Guo *et al.*, 2002; Jin and Liu, 2011; Yang *et al.*, 2012). The initial fabric of loess is determined primarily by gravitational setting and wind strength. Thus, a nearly horizontal principal axis quasi-parallel to bedding planes is likely for loess, but it is not necessary for paleosols because neoformed pedogenic ferrimagnets can form a new fabric independently. Ferrimagnet authigenesis constrained by the sheet structure of phyllosilicates found in this study can account for the preservation of the initial fabric in paleosols. This is supported by strengthening of the original fabric by post-depositional pedogenic ferrimagnets (Bradák *et al.*, 2018).

5. Conclusions

Three sets of loess and mature-paleosol samples from adjacent loess and paleosol units in the CLP have consistent magnetic properties. (1) The samples mainly contain detrital/pedogenic magnetite and hematite particles, and maghemite occurs as rims on the surface of coarse detrital magnetite. (2) SP/SD/vortex state magnetic properties dominate both the loess and paleosol samples. (3) Pedogenic magnetic particles that contribute to the enhancement of both magnetic susceptibility and the frequency dependence of magnetic susceptibility in paleosol samples were present mainly in the medium size (1–10 μm) fractions (host silicates). (4) Most pedogenic magnetite underwent neither high-temperature oxidation during thermal treatment nor low-temperature surface oxidation (maghemitization). (5) Chlorite and muscovite grains are weakly magnetic, with stronger intensities in paleosol

fractions.

Authigenic magnetite and hematite particles occur between muscovite and chlorite phyllosilicate layers in the mature-paleosol medium-grain-sized fraction. The grain size of particles reaches a maximum of a few micrometers for hematite and several hundred nanometers for magnetite. Ultrafine (< a few tens of nanometers) iron-oxide particles are highly concentrated between layers of chlorite grains. The hundreds of nanometer–micron-sized authigenic magnetic particles are concentrated in weathered muscovite/chlorite grains or in aggregates of phyllosilicate fragments. In loess, there are few such magnetic particles, but small amounts of iron-oxide particles finer than these are present in aggregates and on silicate surfaces, in addition to discrete detrital magnetic particles. Authigenic magnetic particles give rise to the magnetizations of muscovite and chlorite. The submicron prism-shaped authigenic magnetite particles with aspect ratios > ~ 4 are probably responsible for paleosol SD and vortex state magnetic properties and magnetic enhancement. Loess and paleosol fractions contain similar concentrations of submicron iron-oxide interspersed on silicate surfaces. Fine/superfine iron-oxide particles are on the surfaces of paleosol silicate grains. The total amount of this iron-oxide is much smaller than that of the hundreds of nanometer authigenic magnetite particles. These finer iron-oxide particles could neither contribute to the SD/vortex state properties nor make a significant contribution to magnetic enhancement in mature paleosols.

Protective silicates account for the low magnetic extraction efficiency and reduce surface oxidation by the surrounding air of pedogenic fine ferrimagnets. Muscovite and chlorite, which account for ~40% of the overall volume of bulk loess/paleosol samples, may be hidden but are likely to be major contributors to magnetic enhancement in mature paleosols.

Acknowledgments

This study was supported by grants 26610162, 22340154, 19340151, and 19K04041 from the Japan Society for the Promotion of Science. Part of this study was performed in collaboration with the Center for Advanced Marine Core Research, Kochi University (reference numbers: 15A001 and 16A002) and with the support of JAMSTEC. We are grateful to M. J. Dekkers (Associate Editor), A. P. Roberts, and an anonymous reviewer for their careful reviews and constructive comments. We thank M. Tobi and K. Takasaki for assistance with fieldwork and A. Miyake, D. Nishio-Hamane, and T. Sakaiya for assistance with laboratory work. Our data are available online (http://www.lib.kobe-u.ac.jp/handle_kernel/90006813).

References

Balsam, W. L., Ellwood, B. B., Ji, J., Williams, E. R., Long, X., & El Hassani, A. (2011).

Magnetic susceptibility as a proxy for rainfall: Worldwide data from tropical and temperate climate. *Quaternary Science Reviews*, *30*, 2732–2744.

Blake, R. L., Hessevick, R. E., Zoltai, T., & Finger, L. W. (1966). Refinement of the hematite structure. *American Mineralogist*, *51*, 123–129.

Bradák, B., Seto, Y., Hyodo, M., & Szeberényic, J. (2018). Relevance of ultrafine grains in the magnetic fabric of paleosols. *Geoderma*, *330*, 125–135.

Borradaile, G. J., & Werner, T. (1994). Magnetic anisotropy of some phyllosilicates. *Tectonophysics*, *235*, 223–248.

Chang, L., Roberts, A. P., Heslop, D., Hayashida, A., Jinhua Li, J., Zhao, X., *et al.* (2016) Widespread occurrence of silicate-hosted magnetic mineral inclusions in marine sediments and their contribution to paleomagnetic recording. *Journal of Geophysical Research: Solid Earth*, *121*, 8415–8431, doi:10.1002/2016JB013109.

Chen, L., Heslop, D., Roberts, A. P., Chang, L., Zhao, X., McGregor, H. V., *et al*. (2017). Remanence acquisition efficiency in biogenic and detrital magnetite and recording of geomagnetic paleointensity. *Geochemistry, Geophysics, Geosystems*, 18, 1435–1450. https://doi.org/10.1002/2016GC006753.

Chen, T., Xie, Q., Xu, H., Chen, J., Ji, J., Lu, H., & Balsam, W. (2010). Characteristics and formation mechanism of pedogenic hematite in Quaternary Chinese loess and paleosols. *Catena*, *81*, 217–225.

Cui, Y., Verosub, K. L., & Roberts, A. P. (1994). The effect of low-temperature oxidation on large multi-domain magnetite, *Geophysical Research Letters*, 21, 757–760.

Deng, C., Zhu, R., Jackson, M. J., Verosub, K. L., & Singer, M. J. (2001). Variability of the Temperature-Dependent Susceptibility of the Holocene Eolian Deposits in the Chinese Loess Plateau: A Pedogenesis Indicator. *Physics and Chemistry of the Earth, Part A: Solid Earth and Geodesy*, *26*, 873–878.

Ding, Z. L., Rutter, N. W., Sun, J. M., Yang, S. L., & Liu, T. S. (2000). Re-arrangement of atmospheric circulation at about 2.6 Ma over northern China: Evidence from grain size records of loess-palaeosol and red clay sequences. *Quaternary Science Reviews*, *19*(6), 547–558.

Evans, M. E., & Heller, F. (1994). Magnetic enhancement and palaeoclimate: Study of a loess/paleosol couplet across the Loess Plateau of China. *Geophysical Journal International*, *117*, 257–264.

Fleet, M. E. (1986). The structure of magnetite: Symmetry of cubic spinel. *Journal of Solid State Chemistry*, *62*, 75–82.

Gatineau, L. (1963). Localisation des remplacements isomorphiques dans la muscovite. *Comptes Rendus Hebdomadaires des Seances de J'Academie des Science*, *256*, 4648–4649.

Goss, C. J. (1987). The kinetics and reaction mechanism of the goethite to hematite

tranformation. *Mineralogical Magazine*, *51*, 437–451.

Guo, B., Zhu, R. X., Florindo, F., Ding, Z. L., & Sun, J. M. (2002). A short, reverse polarity interval within the Jaramillo subchron: Evidence from the Jingbian section, northern Chinese Loess Plateau. *Journal of Geophysical Research: Solid Earth*, *107*(B6), 2124. https://doi.org/10.1029/2001JB000706.

Halpin, J. A., Jensen, T., McGoldrick, P., Meffre, S., Berry, R. F., Everard, J. L., *et al.* (2014). Authigenic monazite and detrital zircon dating from the Proterozoic Rocky Cape Group, Tasmania: Links to the Belt-Purcell Supergroup, North America. *Precambrian Research*, *250*, 50–67.

Han, J. M., & Jiang, W. Y. (1999). Particle size contributions to bulk magnetic susceptibility in Chinese loess and paleosol. *Quaternary International*, *62*, 103–110.

Harrison, R. J., & Feinberg, J. M. (2008). FORCinel: An improved algorithm for calculating first-order reversal curve distributions using locally weighted regression smoothing. *Geochemistry, Geophysics, Geosystems*, *9*, Q05016. doi:10.1029/2008GC001987

Heider, F., Zitzelsberger, A., & Fabian, K. (1996). Magnetic susceptibility and remanent coercive force in grown magnetite crystals from 0.1 μm to 6 mm. *Physics of the Earth and Planetary Interior*, *93*, 239–256.

Heller, F., & Evans, M. E. (1995). Loess magnetism, *Reviews of Geophysics*, *33*, 211–240.

Heslop, D., Dekkers, M. J., Kruiver, P. P., & van Oorschot, I. H. M. (2002). Analysis of isothermal remanent magnetization acquisition curves using the expectation-maximization algorithm. *Geophysical Journal International*, *148*, 58–64.

Jiang, Z., Liu, Q. S., Roberts, A. P., Barrón, V., Torrent, J., & Zhang, Q. (2018). A new model for transformation of ferrihydrite to hematite in soils and sediments. *Geology*, *46*, 987–990. https://doi.org/10.1130/G45386.1

Jin, C. S., & Liu, Q. S. (2010). Reliability of the natural remanent magnetization recorded in Chinese loess. *Journal of Geophysical Research: Solid Earth*, *115*, B04103. https://doi.org/10.1029/2009JB006703

Jin, C. S., & Liu, Q. S. (2011). Revisiting the stratigraphic position of the Matuyama–Brunhes geomagnetic polarity boundary in Chinese loess. *Palaeogeography Palaeoclimatology Palaeoecology*, *299*, 309–317.

Kang, S., Wang, X. L., Roberts, H. M., Duller, G. A. T., Cheng, P., Lu, Y. C., *et al.* (2018). Late Holocene anti-phase change in the East Asian summer and winter monsoons. *Quaternary Science Reviews*, *188*, 28–36.

Kukla, G. (1987). Loess stratigraphy in central China. *Quaternary Science Reviews*, *6*, 191–219.

Lignie, A., Granier, D., Armand, P., Haines, J., & Papet, P. (2012). Modulation of quartz-like GeO_2 structure by Si substitution: An X-ray diffraction study of $Ge_{1-x}Si_xO_2$ ($0 \leq x < 0.2$) flux-grown single crystals. *Journal of Applied Crystallography*, *45*, 272–278.

Liu, Q. S., Banerjee, S. K., Jackson, M. J., Chen, F. H., Pan, Y. X., & Zhu, R. X. (2003). An integrated study of the grain-size-dependent magnetic mineralogy of the Chinese loess/paleosol and its environmental significance. *Journal of Geophysical Research: Solid Earth*, *108*, B92437. https://doi.org/10.1029/2002JB002264

Liu, Q. S., Jackson, M. J., Banerjee, S. K., Maher, B. A., Deng, C. L., Pan, Y. X., *et al.* (2004). Mechanism of the magnetic susceptibility enhancements of the Chinese loess. *Journal of Geophysical Research: Solid Earth*, *109*, B12107. https://doi.org/10.1029/2004JB003429

Liu, Q. S., Torrent, J., Maher, B. A., Yu, Y., Deng, C. L., Zhu, R. X., *et al.* (2005). Quantifying grain size distribution of pedogenic magnetic particles in Chinese loess and its significance for pedogenesis. *Journal of Geophysical Research: Solid Earth*, *110*, B11102. https://doi.org/10.1029/2005JB/003726

Liu, Q. S., Deng, C. L., Torrent, J., & Zhu, R. X. (2007). Review of recent developments in mineral magnetism of the Chinese loess. *Quaternary Science Reviews*, *26*, 368–385.

Liu, X. M., Liu, T. S., Xu, T. C., Liu, C., & Chen, M. Y. (1988). The Chinese loess in Xifeng, I. The primary study on magnetostratigraphy of a loess profile in Xifeng area, Gansu province. *Geophysical Journal*, *92*, 345–348.

Le Caër, S., Lima, M. Gosset, D. Simeone, D. Bergaya, F. Pommeret, S., *et al.* (2012). Dynamics of Water Confined in Clay Minerals. *Journal Physical Chemistry C*, *116*(23), 12916–12925.

Maher, B. A. (2016). Palaeoclimatic records of the loess/palaeosol sequences of the Chinese Loess Plateau. *Quaternary Science Reviews*, *154*, 23–84. https://doi.org/10.1016/j.quascirev.2016.08.004

Maher, B. A., & Thompson, R. (1991). Mineral magnetic record of the Chinese loess and paleosols. *Geology*, *19*, 3–6.

Maher, B. A., & Thompson, R. (1992). Paleoclimatic significance of the mineral magnetic record of the Chinese loess and paleosols. *Quaternary Research*, *37*, 155–170.

Maher, B. A., Thompson, R., & Zhou, L. P. (1994). Spatial and temporal reconstructions of changes in the Asian palaeomonsoon: A new mineral magnetic approach. *Earth and Planetary Science Letters*, *125*, 461–471.

Maher, B. A., & Thompson, R. (1995). Paleorainfall reconstructions from pedogenic magnetic susceptibility variations in the Chinese loess and paleosols. *Quaternary Research*, *44*, 383–391.

Martín-Hernández, F., & Hirt, A. M. (2003). The anisotropy of magnetic susceptibility in biotite, muscovite and chlorite single crystals. *Tectonophysics*, *367*, 13–28.

Mishima, T., Hyodo, M. Tanigawa, K., Katoh, S., Yang, T. S., & Yang, Z. Y. (2015). Multiple rapid polarity swings within the Gauss-Matuyama geomagnetic transition record from Lingtai, central Loess Plateau, China. *XIX INQUA Congress abstract*, T01469.

Morad, S. (1986). SEM study of authigenic rutile, anatase and broockite in Proterozoic

sandstones from Sweden. *Sedimentary Geology*, *46*, 77–89.

Muxworthy, A. R., & Williams, W. (2009). Critical superparamagnetic/single domain grain sizes in interacting magnetite particles: Implications for magnetosome crystals. *Journal of the Royal Society Interface*, *6*(41), 1207–1212. https://doi.org/10.1098/rsif.2008.0462

Nishiyama, T. (1983). Mineralogical aspect of mica minerals. *Journal of Clay Science Society of Japan*, *23*, 39–45 (in Japanese).

Pike, C. R., Roberts, A. P., & Verosub, K. L. (1999). Characterizing interactions in fine magnetic particle systems using first order reversal curves. *Journal of Applied Physics*, *85*, 6660–6667.

Pike, C. R., Roberts, A. P., & Verosub, K. L. (2001). FORC diagrams and thermal relaxation effects in magnetic particles. *Geophysical Journal International*, 145, 721–730.

Porter, S. C., & An, Z. (1995). Correlation between climate events in the North Atlantic and China during the last glaciation. *Nature*, *375*, 305–308.

Ribbe, P. H., Megaw, H. D., Taylor, W. H., Ferguson, R. B., & Traill, R. J. (1969). The albite structure. *Acta Crystallographica*, *B25*, 1503–1518.

Roberts, A. P. (2015). Magnetic mineral diagenesis. *Earth-Science Reviews*, *151*, 1–47.

Roberts, A. P., Pike, C. R., & Verosub, K. L. (2000). First-order reversal curve diagrams: A new tool for characterizing the magnetic properties of natural samples. *Journal of Geophysical Research: Solid Earth*, *105*, 28461–28475.

Seto, Y., Nishio-Hamane, D., Nagai, T., & Sata, N. (2010). Development of a software suite on X-ray diffraction experiments. *The Review of High Pressure Science and Technology*, *20*, 269–276.

Spassov, S., Heller, F., Kretzschmar, R., Evans, M. E., Yue, L. P., & Nourgaliev, D. K. (2003). Detrital and pedogenic magnetic mineral phases in the loess/palaeosol sequence at Lingtai (Central Chinese Loess Plateau). *Physics of the Earth and Planetary Interior*, *140*, 255–275.

Sun, Y. B., Clemens, S. C., An, Z. S., & Yu, Z. W. (2006). Astronomical timescale and palaeoclimatic implication of stacked 3.6-Myr monsoon records from the Chinese Loess Plateau. *Quaternary Science Reviews*, *25*, 33–48.

Sun, W. W., Banerjee, S. K., & Hunt, C. P. (1995). The role of maghemite in the enhancement of magnetic signal in the Chinese loess-paleosol sequence: An extensive rock magnetic study combined with citrate-bicarbonate-dithionite treatment. *Earth and Planetary Science Letters*, *133*, 493–505.

Toby, B. H., & Von Dreele, R. B. (2013). GSAS-II: The genesis of a modern open-source all purpose crystallography software package. *Journal of Applied Crystallography*, *46*, 544–549.

Ueno, Y., Hyodo, M., Yang, T. S., & Katoh, S. (2019). Intensified East Asian winter monsoon during the last geomagnetic reversal transition. *Scientific Reports*, *9*, 9389.

van Oorschot, I. H. M., & Dekkers, M. J. (1999). Dissolution behavior of fine grained magnetite and maghemite in the citrate-bicarbonate-dithionite extraction method. *Earth and Planetary Science Letters*, *167*, 283–295.

van Velzen, A. J., & Dekkers, M. J. (1999). Low-temperature oxidation of magnetite in loess-paleosol sequences: A correction of rock magnetic parameters. *Studia Geophysica et Geodaetica*, *43*, 357–375.

van Velzen, A. J., & Zijderveld, J. D. A. (1995). Effects of weathering on single-domain magnetite in Early Pliocene marine marls. *Geophysical Journal International*, *121*, 267–278.

Verosub, K. L., Fine, P., Singer, M. J., & TenPas, J. (1993). Pedogenesis and paleoclimate: Interpretation of the magnetic susceptibility record of Chinese loess-paleosol sequences. *Geology*, *21*, 1011–1014.

Vidic, N. J., TenPas, J. D., Verosub, K. L., & Singer, M. J. (2000). Separation of pedogenic and lithogenic components of magnetic susceptibility in the Chinese loess/palaeosol sequence as determined by the CBD procedure and a mixing analysis. *Geophysical Journal International*, *142*, 551–562.

Yang, S., Ding, Z., Li, Y. Y., Wang, X., Jiang, W. Y., & Huang, X. F. (2015). Warming-induced northwestward migration of the East Asian monsoon rain belt from the Last Glacial Maximum to the mid-Holocene. *Proceedings of the National Academy of Sciences of the United States of America*, *112*, 13178–13183.

Yang, T. S., Hyodo, M., Yang, Z. Y., Ding, L., Li, H. D., Fu, J. L., *et al.* (2008). Latest Olduvai short-lived reversal episodes recorded in Chinese loess. *Journal of Geophysical Research: Solid Earth*, *113*, B05103. https://doi.org/10.1029/2007JB005264

Yang, T. S., Hyodo, M., Yang, Z. Y., Li, H. D., & Maeda, M. (2010). Multiple rapid polarity swings during the Matuyama-Brunhes transition from two high-resolution loess-paleosol records. *Journal of Geophysical Research: Solid Earth*, *115*, B05101. https://doi.org/10.1029/2009JB006301

Yang, T. S., Hyodo, M., Zhang, S. H., & Maeda, M. (2013). New insights into magnetic enhancement mechanism in Chinese paleosols. *Palaeogeography Palaeoclimatology Palaeoecology*, *369*, 493–500.

Yang, T. S., Li, H., Wu, H., Yang, Z. Y., Zhang, S. H., & Hyodo, M. (2012). Reliability of relative paleointensity recorded in Chinese loess-paleosol sediments. *Acta Geologica Sinica (English Edition)*, *86*, 1276–1288.

Zhou, L. P., Oldfield, F., Wintle, A. G., Robinson, S. G., & Wang, J. T. (1990). Partly pedogenic origin of magnetic variations in Chinese loess. *Nature*, *346*, 737–739.

Zheng, H., & Bailey, S. W. (1989). Structures of intergrowth triclinic and monoclinic IIb chlorites from Kenya. *Clays and Clay Minerals*, *37*, 308–316.

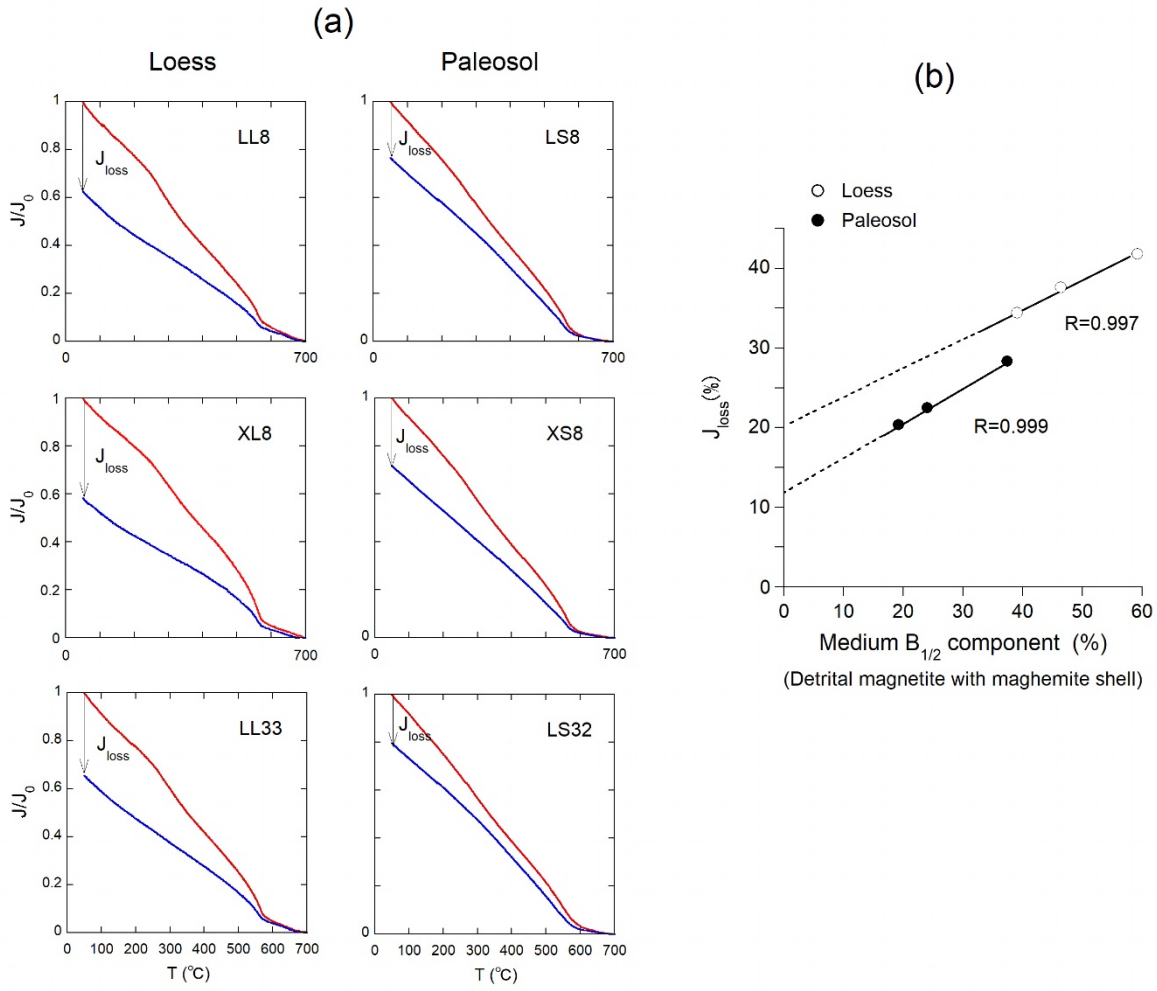

Figure 1. Thermomagnetic results. (a) Heating (red) and cooling (blue) curves. (b) Plot of magnetization loss (%) after cooling versus the medium $B_{1/2}$ component (component 2) of isothermal remnant magnetization (IRM, %) in Table S1. $B_{1/2}$: the field at which half of the saturation IRM is reached (Heslop *et al.*, 2002).

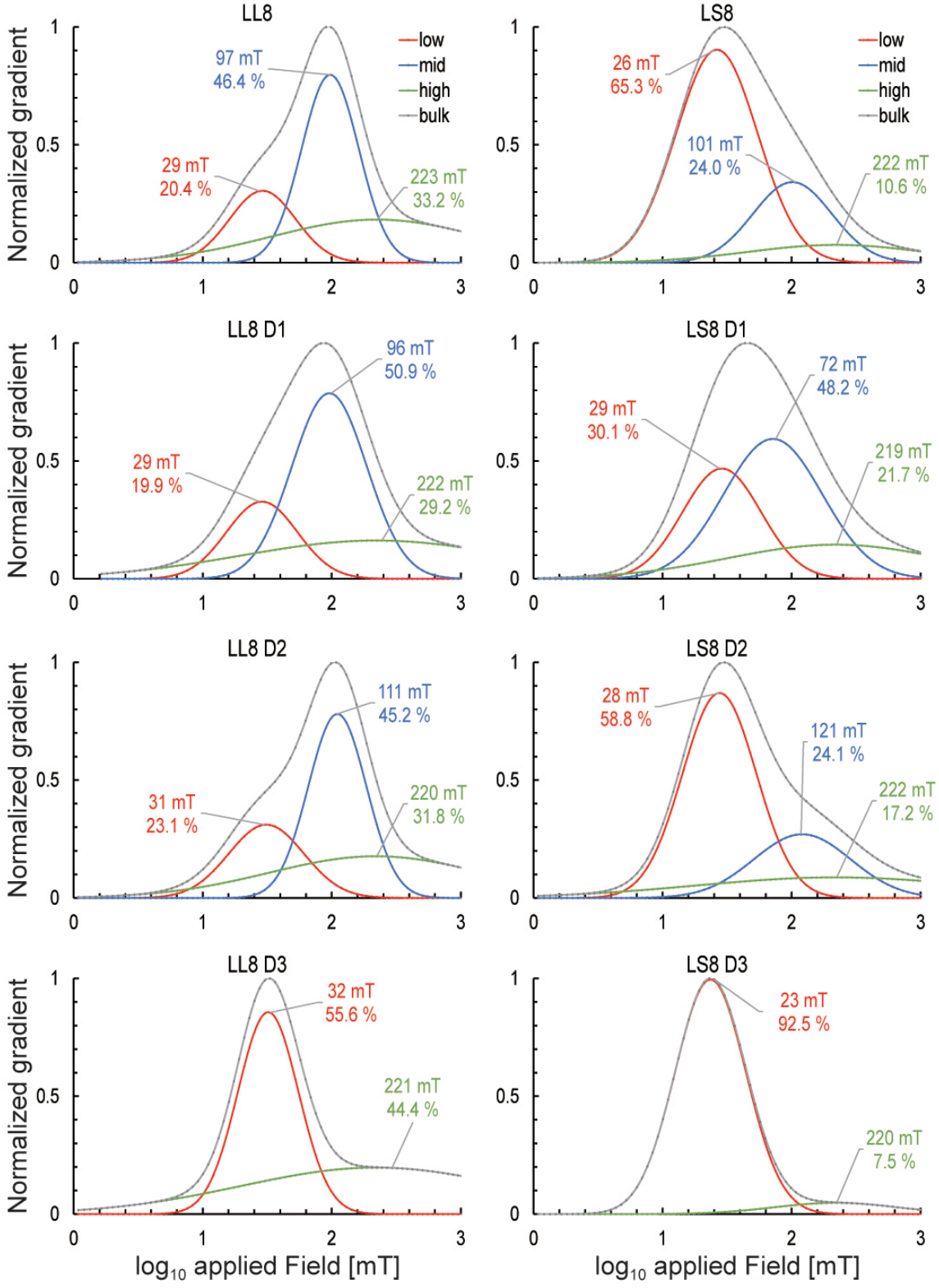

Figure 2. Results of isothermal remnant magnetization (IRM) component analyses for the bulk, D1, D2, and D3 samples of the LL8 loess and LS8 paleosol fractions. The low, medium, and high $B_{1/2}$ components are indicated by red, blue, and green curves, respectively. The gradient maxima (mT) and contribution (%) toward saturation IRM are also shown.

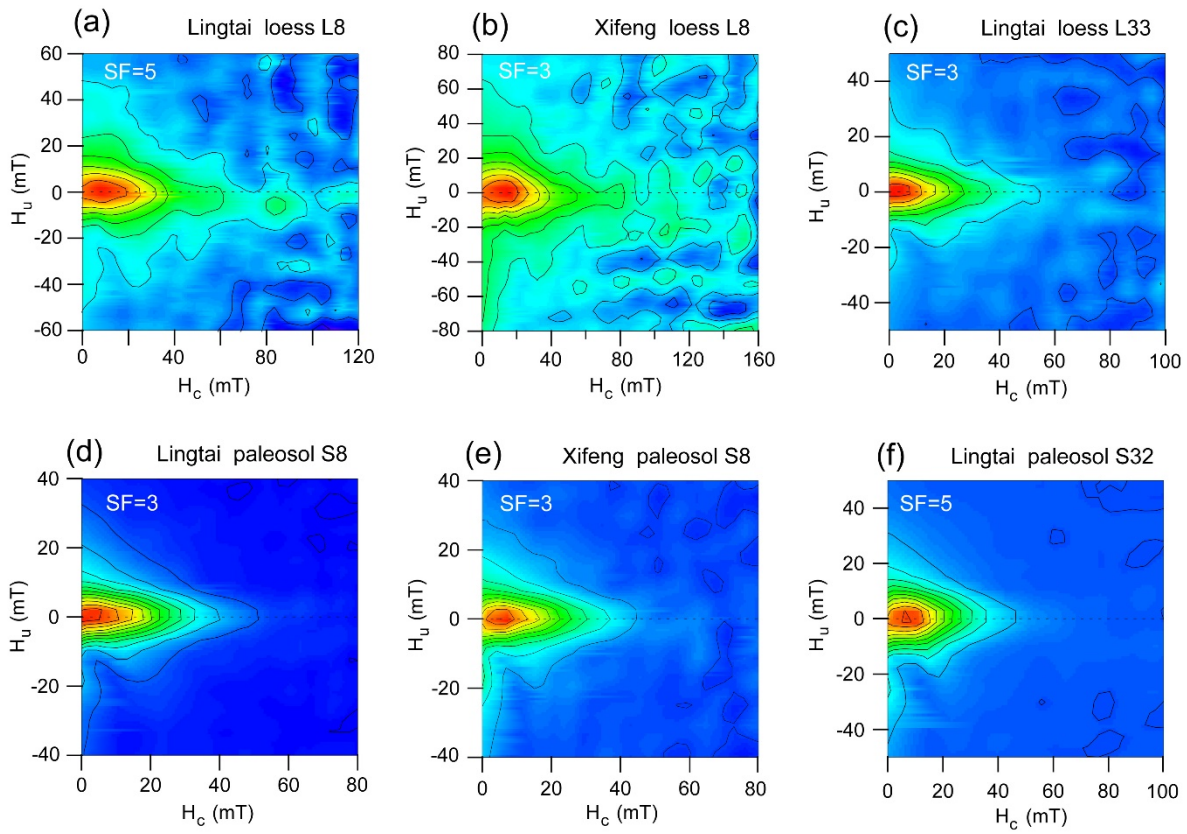

Figure 3. First-order reversal curve (FORC) diagrams for loess and paleosol samples from Lingtai and Xifeng, Chinese Loess Plateau. The samples are from Lingtai loess L8 (a), Xifeng loess L8 (b), Lingtai loess L33 (c), Lingtai paleosol S8 (d), Xifeng paleosol S8 (e), and Lingtai paleosol (f) layers.

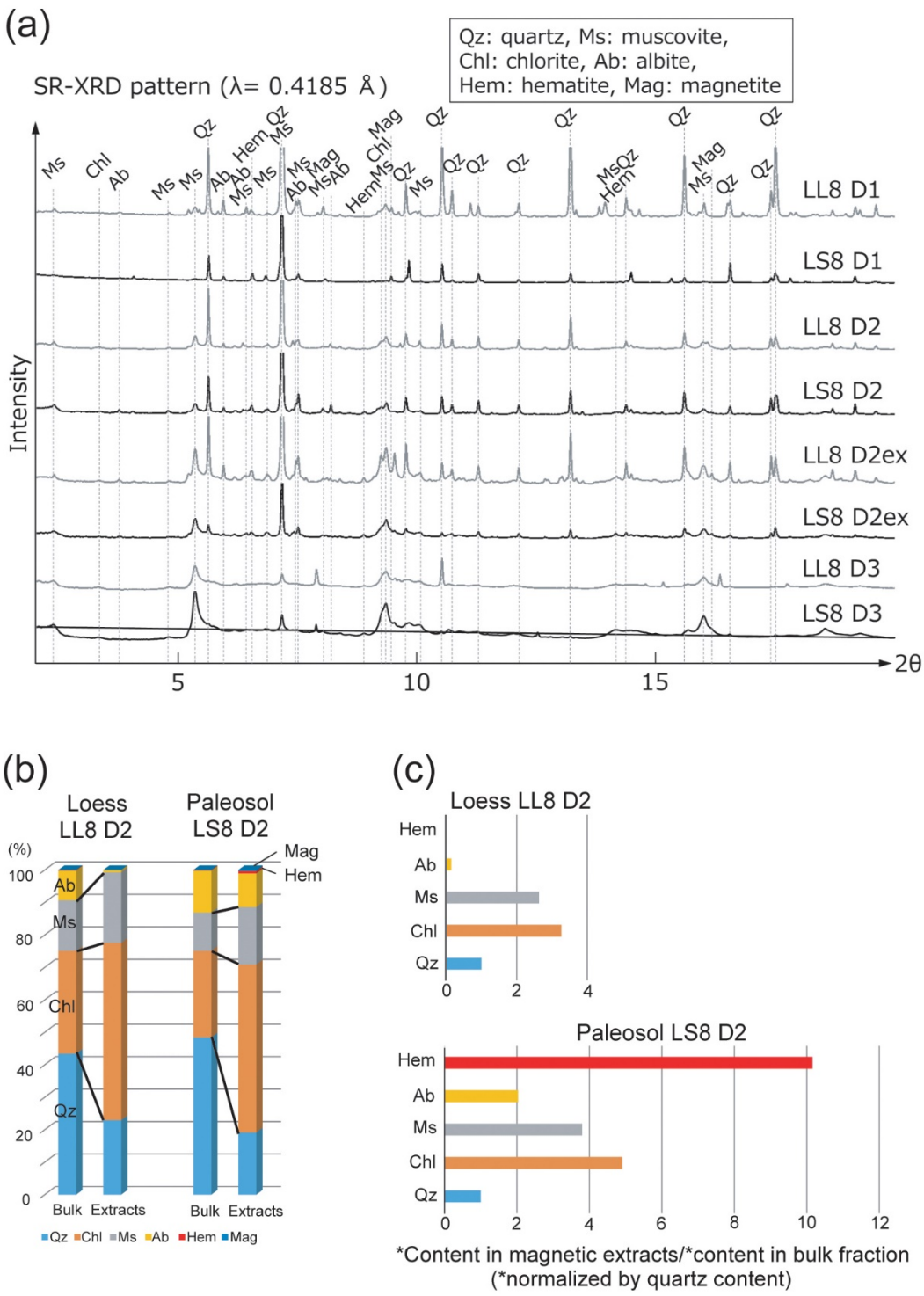

Figure 4. Results of synchrotron radiation X-ray diffraction (XRD) analyses and Rietveld refinements. (a) XRD patterns. Magnetite and maghemite are indistinguishable due to their similar crystal structure. (b) Mineral contents by volume (%; Table 2). Higher muscovite and chlorite contents are found in magnetic extracts. (c) Effects of magnetic extraction. The content of each mineral after separation, relative to that before separation, was calculated using values normalized to quartz content.

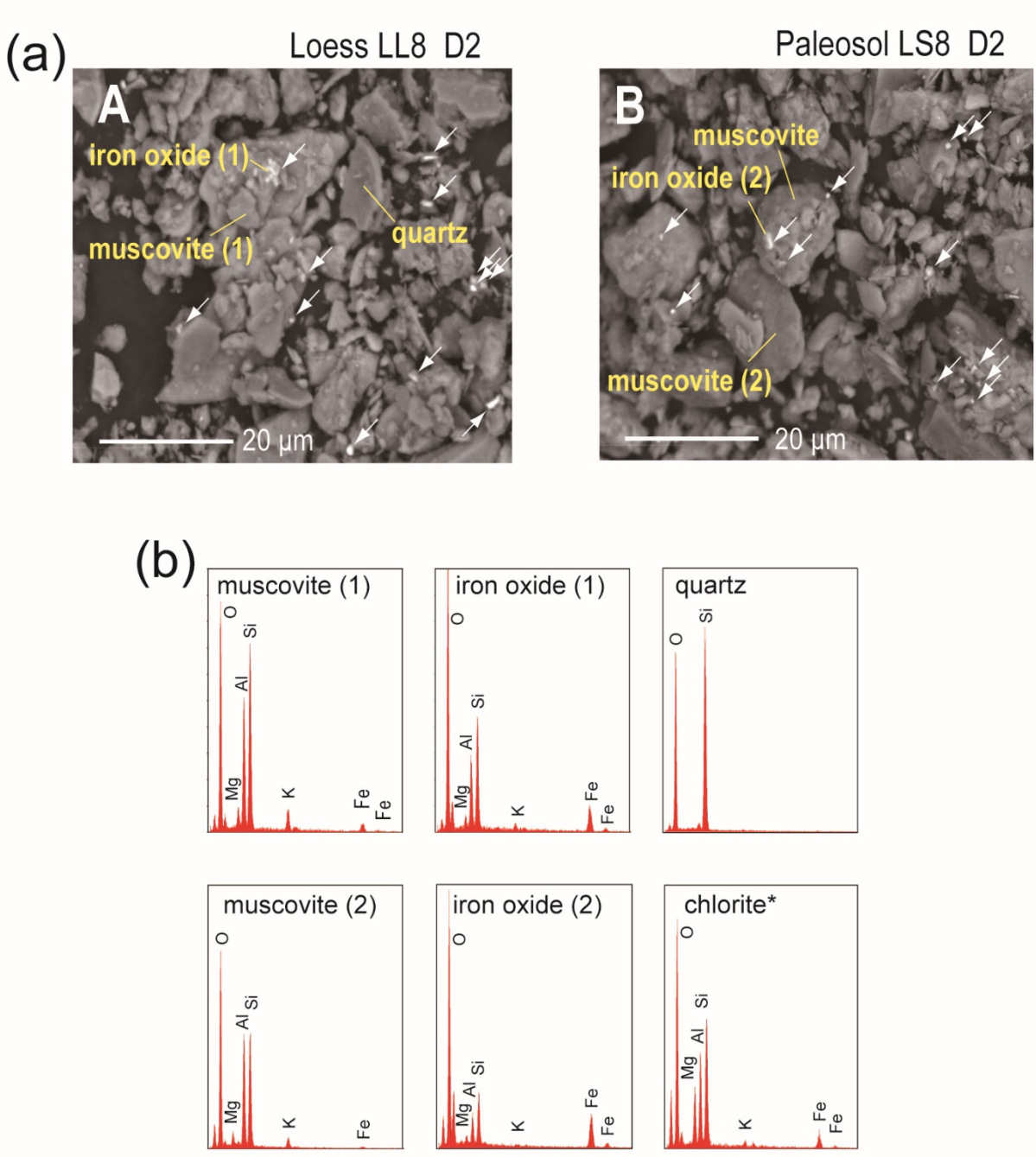

Figure 5. Results of scanning electron microscope (SEM) observations with the LL8 loess and LS8 paleosol samples. (a) Backscattered electron images. White arrows on the images indicate possible iron-oxides. (b) Energy dispersive X-ray spectrometry data for the grains indicated on the SEM images in (a) and for the chlorite* grain indicated on the SEM image in Figure S2 (c).

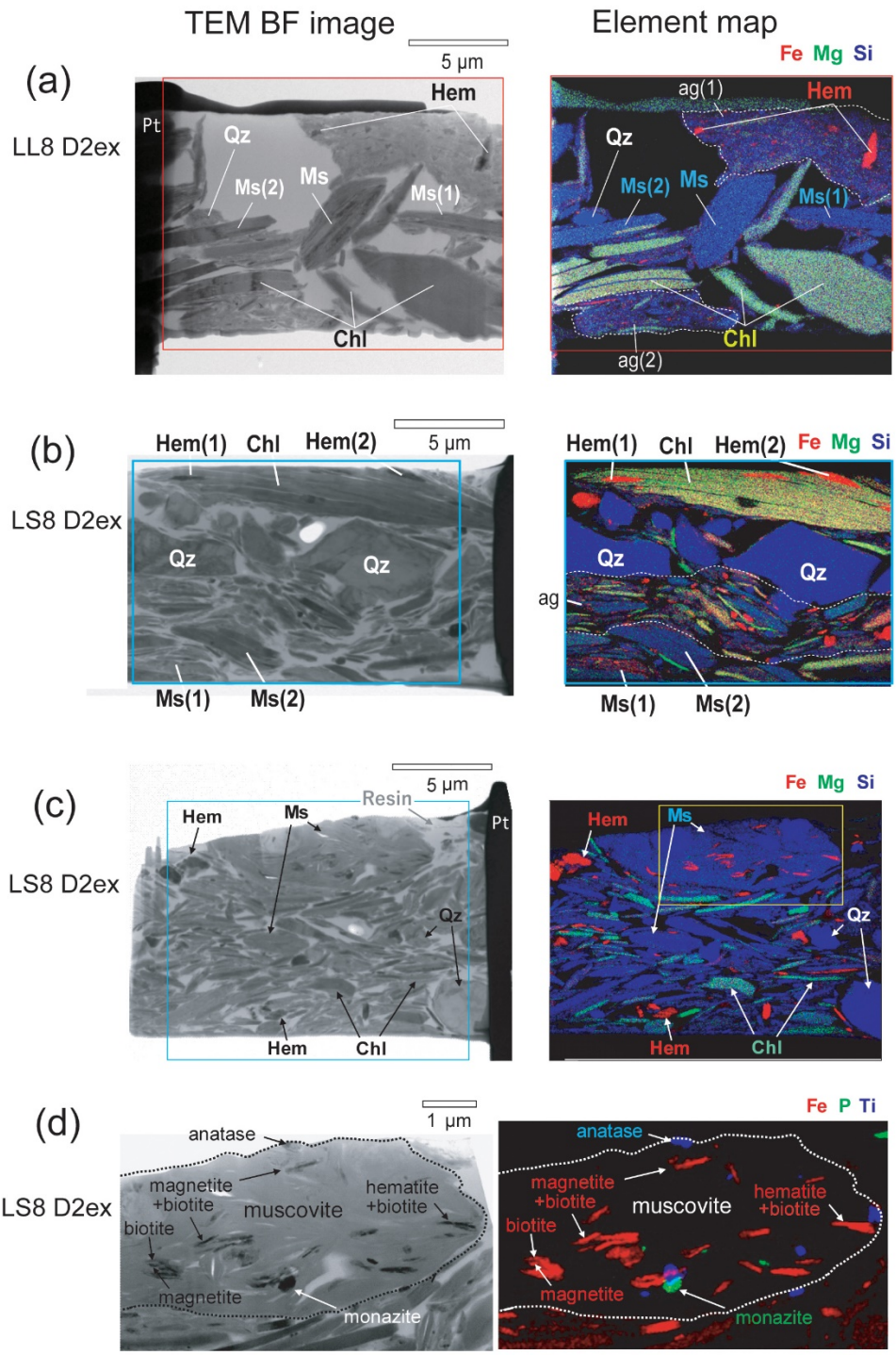

Figure 6. Results of transmission electron microscope (TEM) observations. Bright field (BF) TEM image and combined X-ray map for Fe (red), Mg (green), and Si (blue) for (a) the D2 LL8 loess (magnetic extracts) and (b)(c) D2 LS8 paleosol (magnetic extracts) samples. (d) BF TEM image and combined X-ray map for Fe (red), P (green), and Si (blue) of the area in (c). ag: aggregate; ag (1, 2): aggregate (1, 2); Ms: muscovite; Ms (1, 2): muscovite (1, 2); Chl: chlorite; Hem: hematite; Hem (1, 2): hematite (1, 2); Qz: quartz.

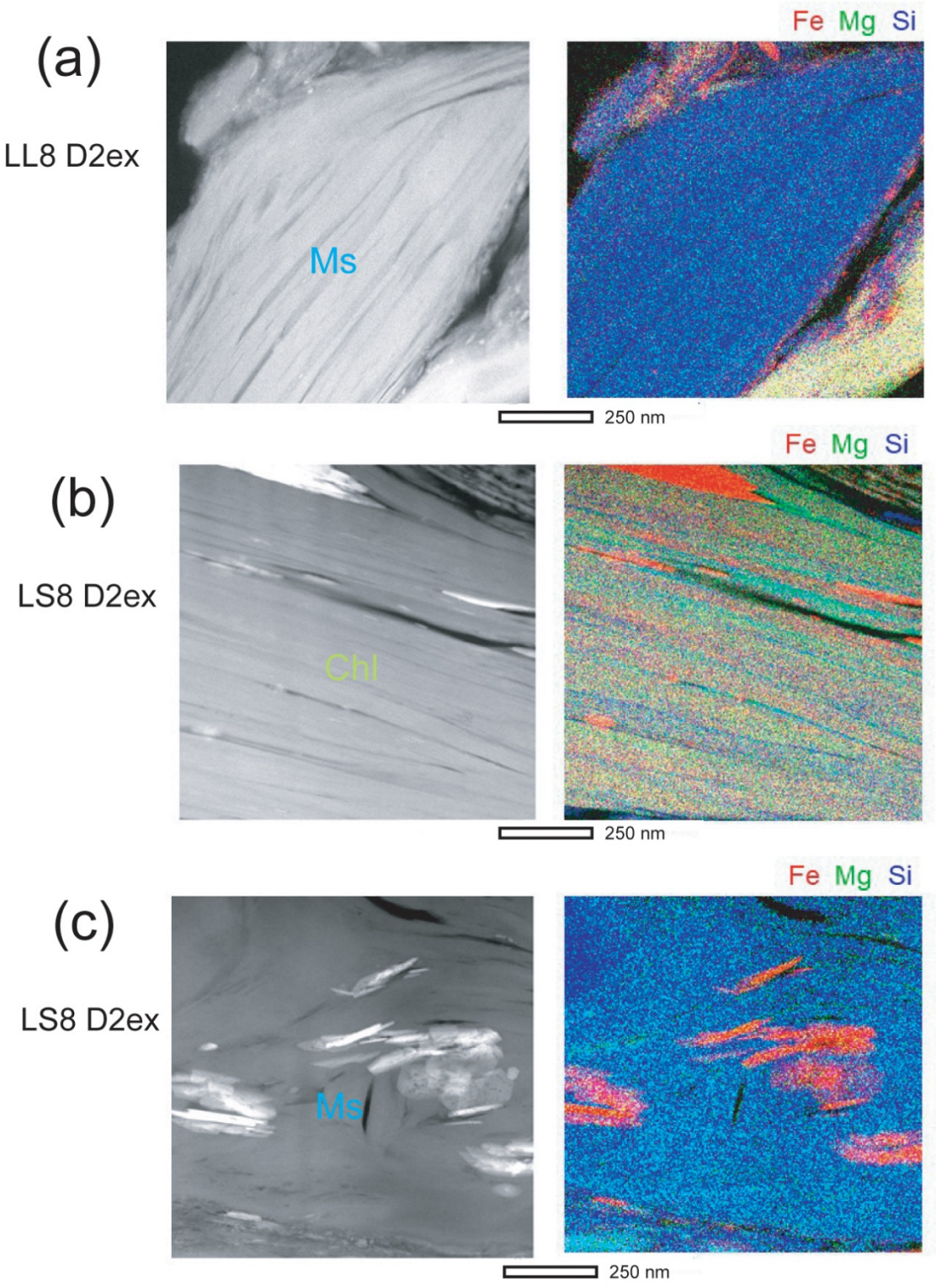

Figure 7. Results of scanning TEM (STEM) observations. Dark field (DF) STEM image (left) and combined X-ray map of Fe (red), Mg (green), and Si (blue) (right) for (a) the D2 LL8 loess (magnetic extracts) and (b)(c) D2 LS8 paleosol (magnetic extracts) samples. Ms: muscovite; Chl: chlorite.

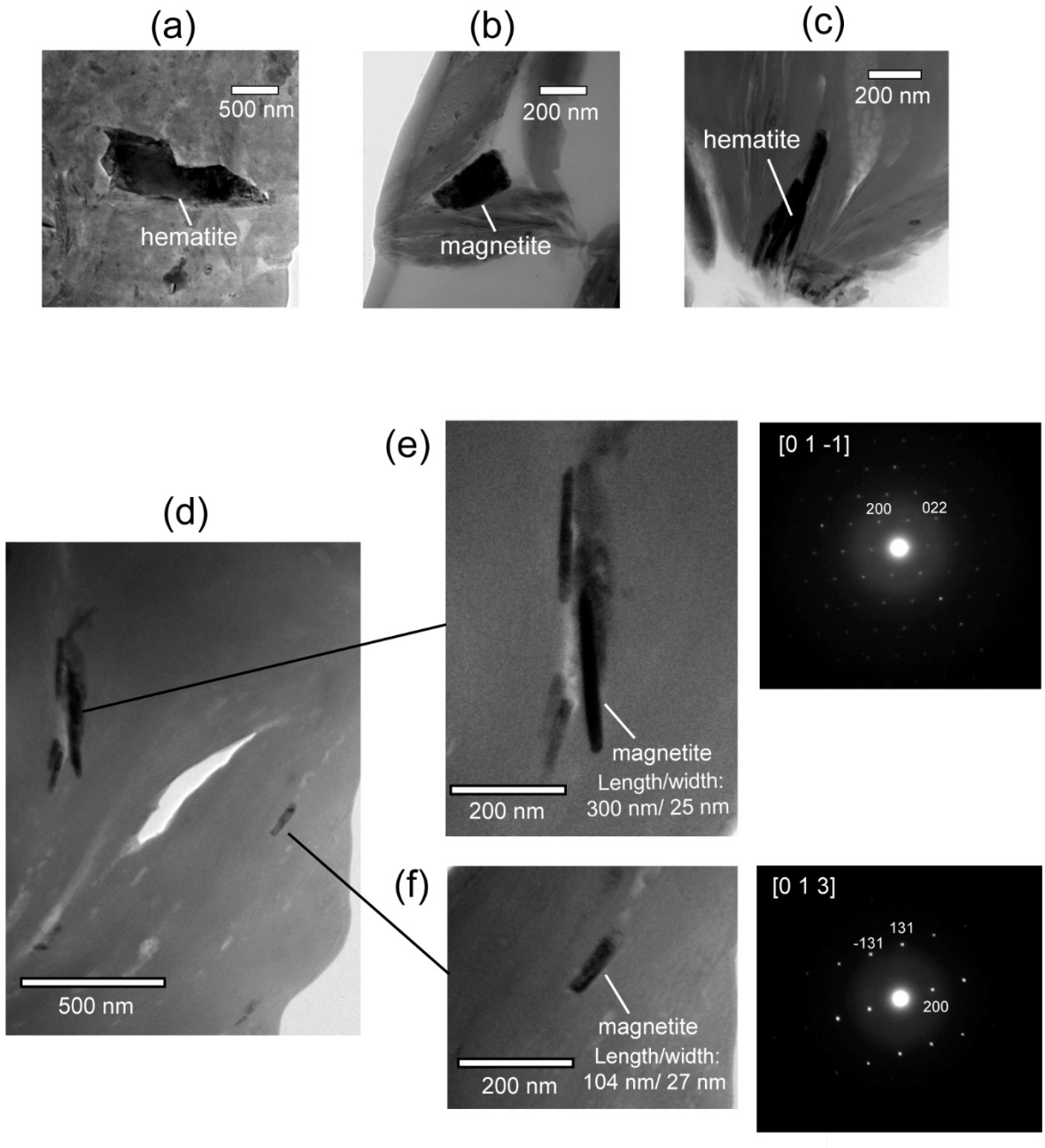

Figure 8. TEM images. Bright field (BF) TEM images of discrete (a) hematite and (b) magnetite particles in the loess sample. BF TEM images of authigenic (c) hematite and (d) magnetite particles included in the weathered muscovite of the paleosol sample. (e, f) Enlarged BF TEM images and electron diffraction patterns of authigenic magnetite particles in (d).

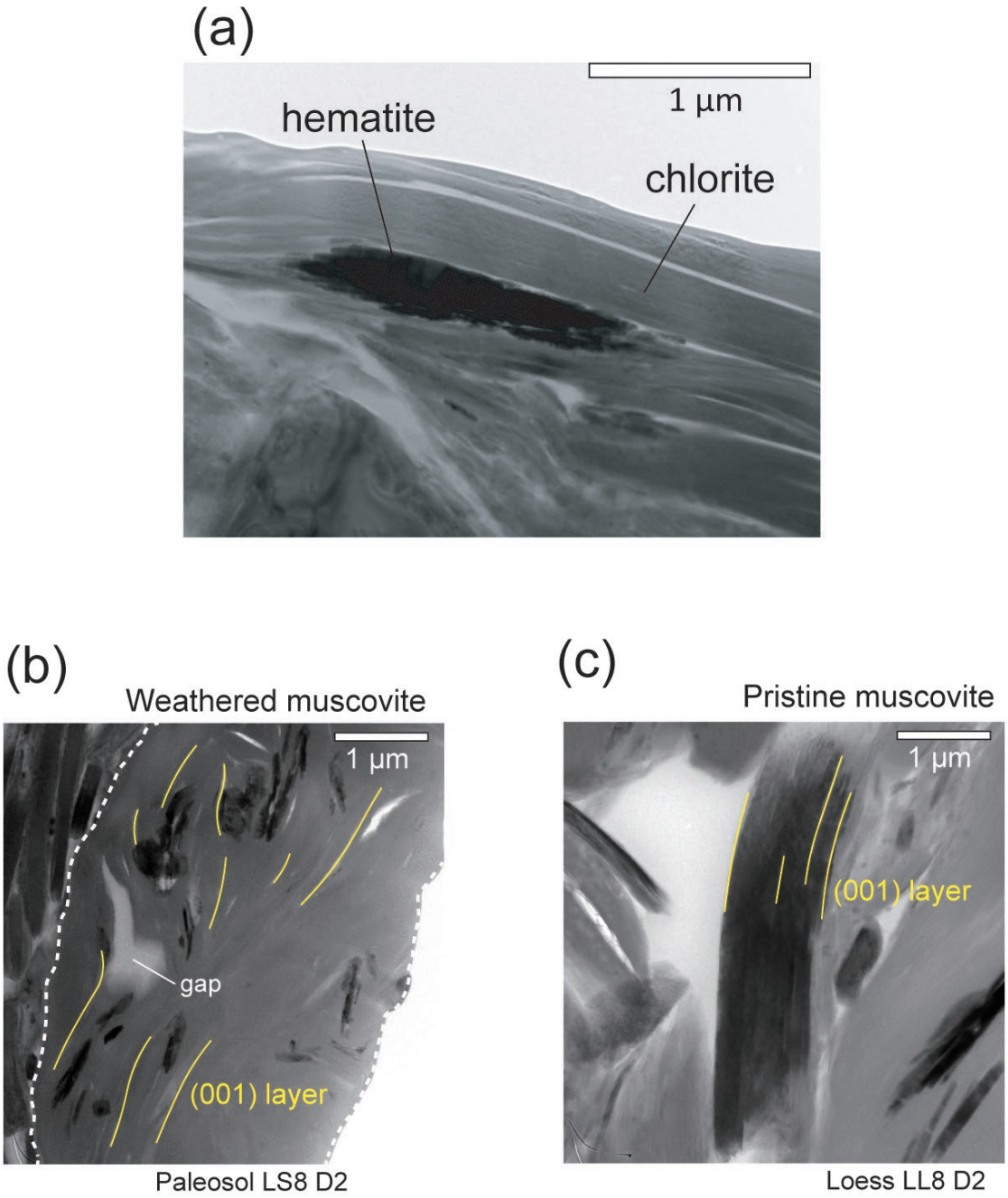

Figure 9. Bright field (BF) TEM images of (a) a weathered chlorite grain with an authigenic hematite particle, (b) a weathered muscovite grain with authigenic iron oxide, and (c) a pristine muscovite grain.

Table 1. Mass, magnetic susceptibility (χ), and frequency dependence of χ (χ_{FD}, χ_{FD}%, mass χ_{FD}).

Sample ID		Mass		Mass χ	**Volume χ		χ_{FD} (χ_{500Hz}-χ_{16kHz})		χ_{FD}% (χ_{500Hz}–χ_{16kHz})/χ_{500Hz}	Mass χ_{FD}
	Bulk/ fraction		Contr. to bulk	χ_{500Hz}	χ_{500Hz}	Contr. to bulk		Contr. to bulk		
		g	%	$10^{-8}m^3/kg$	10^{-5}SI	%	10^{-5}SI	%	%	$10^{-8}m^3/kg$
Lingtai L8										
LL8	Bulk	2.003		28.9	5.20		0.57		10.9	3.2
	D1	0.943	47.1	10.6	0.90	17.3	0.10	17.4	11.0	1.2
	D2	0.892	44.5	31.7	2.54	48.8	0.27	48.2	10.8	3.4
	*D3	0.098	4.9	-	-	-	-			
	(loss)	(0.07)	(3.5)	-	-	(< 32.9)	-			
Lingtai S8										
LS8	Bulk	2.011		115.4	20.83		3.21		15.4	17.8
	D1	0.939	46.7	48.0	4.04	19.4	0.68	21.2	16.8	8.1
	D2	0.932	46.3	129.5	10.83	52.0	1.89	58.9	17.5	22.6
	D3	0.130	6.5	243.7	2.84	13.6	0.52	16.2	18.4	44.8
	(loss)	(0.011)	(0.5)	(3274.2)	(3.13)	(15.0)	(0.12)	(16.5)		
Xifeng L8										
XL8	Bulk	2.079		18.4	3.43		0.58		16.8	3.1
	D1	1.243	59.8	10.3	1.15	33.6	0.10	73.9	8.4	0.9
	D2	0.741	35.6	8.1	0.54	15.6	0.20	22.9	37.3	3.0
	*D3	0.039	1.9	-	-	-	-			
	(loss)	(0.056)	(2.7)	-	-	(< 50.8)	-			
Xifeng S8										
XS8	Bulk	2.004		115.8	20.81		3.52		16.9	19.6
	D1	1.103	55.0	69.3	6.86	28.2	1.08	27.1	15.8	10.9
	D2	0.751	37.5	121.0	8.15	44.0	1.24	63.5	15.2	18.4
	D3	0.099	4.9	228.3	2.03	9.7	0.65	6.6	31.8	72.7
	(loss)	(0.051)	(2.5)	(826.9)	(3.77)	(18.1)	(0.55)	(2.7)		
Lingtai L33										
LL33	Bulk	1.997		31.9	5.71		1.38		24.2	7.7
	D1	0.916	45.9	26.9	2.21	38.7	0.44	31.9	19.9	5.4
	D2	0.980	49.1	36.1	3.17	55.5	0.89	64.5	28.1	10.1
	*D3	0.040	2.0	-	-		-			
	(loss)	(0.061)	(3.0)	-	-	(< 5.8)	-			
Lingtai S32										
LS32	Bulk	2.000		176.6	31.69		6.33		20.0	35.3
	D1	0.602	30.1	66.5	3.59	11.3	0.81	12.8	22.6	15.0
	D2	1.126	56.3	201.7	20.38	64.3	3.94	62.2	19.3	39.0
	D3	0.206	10.3	337.8	6.23	19.7	1.38	21.8	22.2	74.8
	(loss)	(0.067)	(3.3)	(248.5)	(1.49)	(4.7)	(0.2)	(3.2)		

*χ for D3 of each loess sample is unmeasurable because of its extremely low value.

**Volume χ was calculated assuming the same volume as the bulk sample.

D1 (> 10 μm), D2 (1-10 μm), D3 (< 1 μm)

Table 2. Results of the Rietveld refinement.

	D2 (vol %)				D3 (vol %)	
	LL8		LS8		LL8	LS8
Mineral	Bulk	Extracts	Bulk	Extracts	Bulk	Bulk
Quartz	42.7	20.5	48.4	19.2	3.6	1.8
Muscovite	31.2	48.4	26.7	51.7	61.0	61.9
Chlorite	15.3	19.3	11.8	17.7	31.9	24.9
Albite	10.8	11.3	12.9	10.4	3.1	10.6
Hematite	-	0.73	0.19	0.75	0.44	0.88
Magnetite	-	-	-	0.31	-	-

LL8: Lingtai loess L8, LS8: Lingtai paleosol S8

D2 (1–10 μm), D3 (< 1 μm)

Journal of Geophysical Research: Solid Earth

Supporting Information for

Nano-sized authigenic magnetite and hematite particles in mature-paleosol phyllosilicates: New evidence for a magnetic enhancement mechanism in loess sequences of China

Masayuki Hyodo[1,2], Takuroh Sano[2], Megumi Matsumoto[3,4], Yusuke Seto[2], Balázs Bradák[1,5], Kota Suzuki[2], Jun-ichi Fukuda[1], Meinan Shi[6], Tianshui Yang[7]

[1] Research Center for Inland Seas, Kobe University, Kobe 657-8501, Japan

[2] Department of Planetology, Kobe University, Kobe 657-8501, Japan

[3] Center for Supports to Research and Education Activities, Kobe University, Kobe 657-8501, Japan

[4] Department of Earth and Planetary Materials Science, Tohoku University, Sendai 980-8578, Japan

[5] Department of Physics, EPS, University of Burgos, 09006 Burgos, Spain

[6] School of Ocean Sciences, China University of Geosciences, Beijing 100083, China

[7] School of Earth Sciences and Resources, China University of Geosciences, Beijing 100083, China

Contents of this file

Introduction

This supporting information provides the figures and the table cited in the main article.

Corresponding author: Masayuki Hyodo, mhyodo@kobe-u.ac.jp

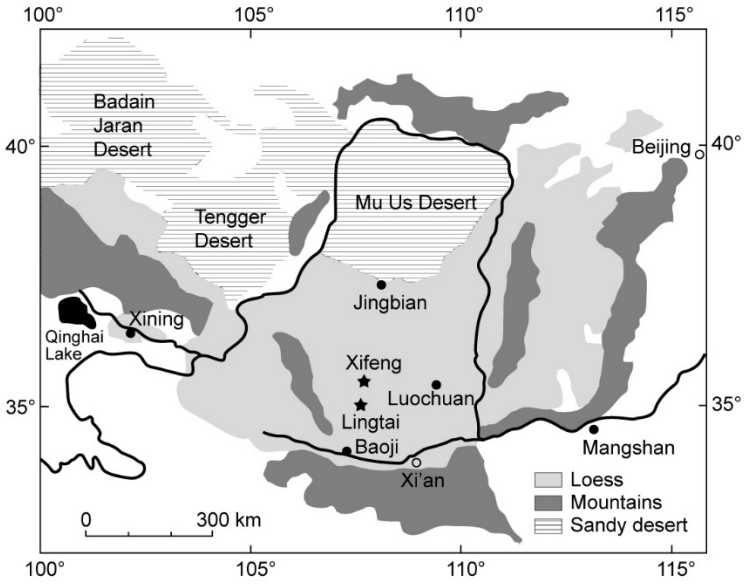

Figure S1. Map with sample sites on the Chinese Loess Plateau. Sample sites for this study are indicated by stars. Data from previous studies are indicated by solid circles (see text).

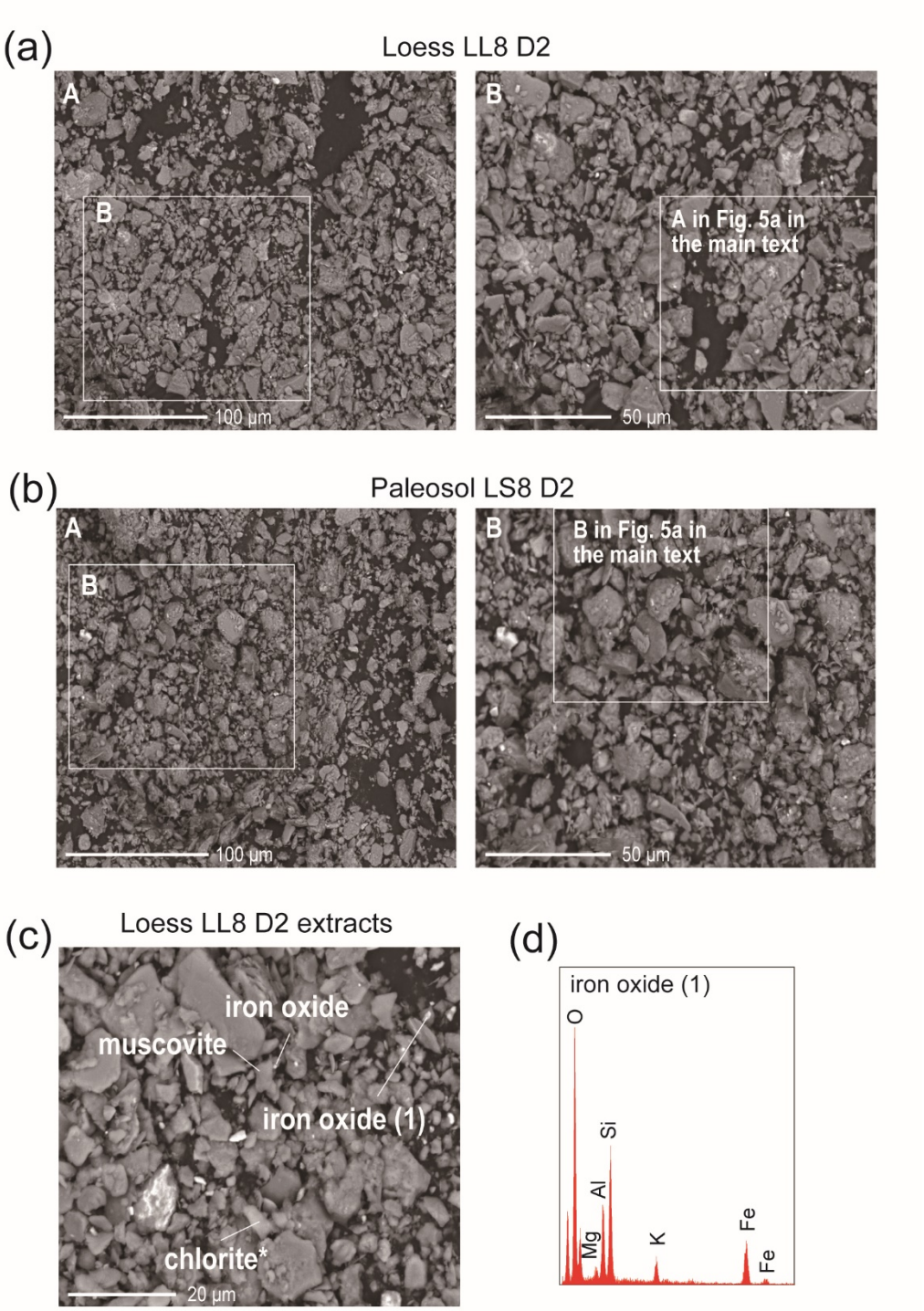

Figure S2. Results of scanning electron microscope (SEM) experiments. Backscattered electron images of the (a) D2 LL8 loess and (b) D2 LS8 paleosol samples. The square B in (a) and (b) indicates the areas labeled A and B in Figure 5a, respectively. (c) Backscattered electron images of the D2 LL8 loess extracts. Energy dispersive X-ray spectrometry (EDS) data for chlorite* are shown in Figure 5. (d) EDS data for iron oxide (1) observed in the SEM image in (c).

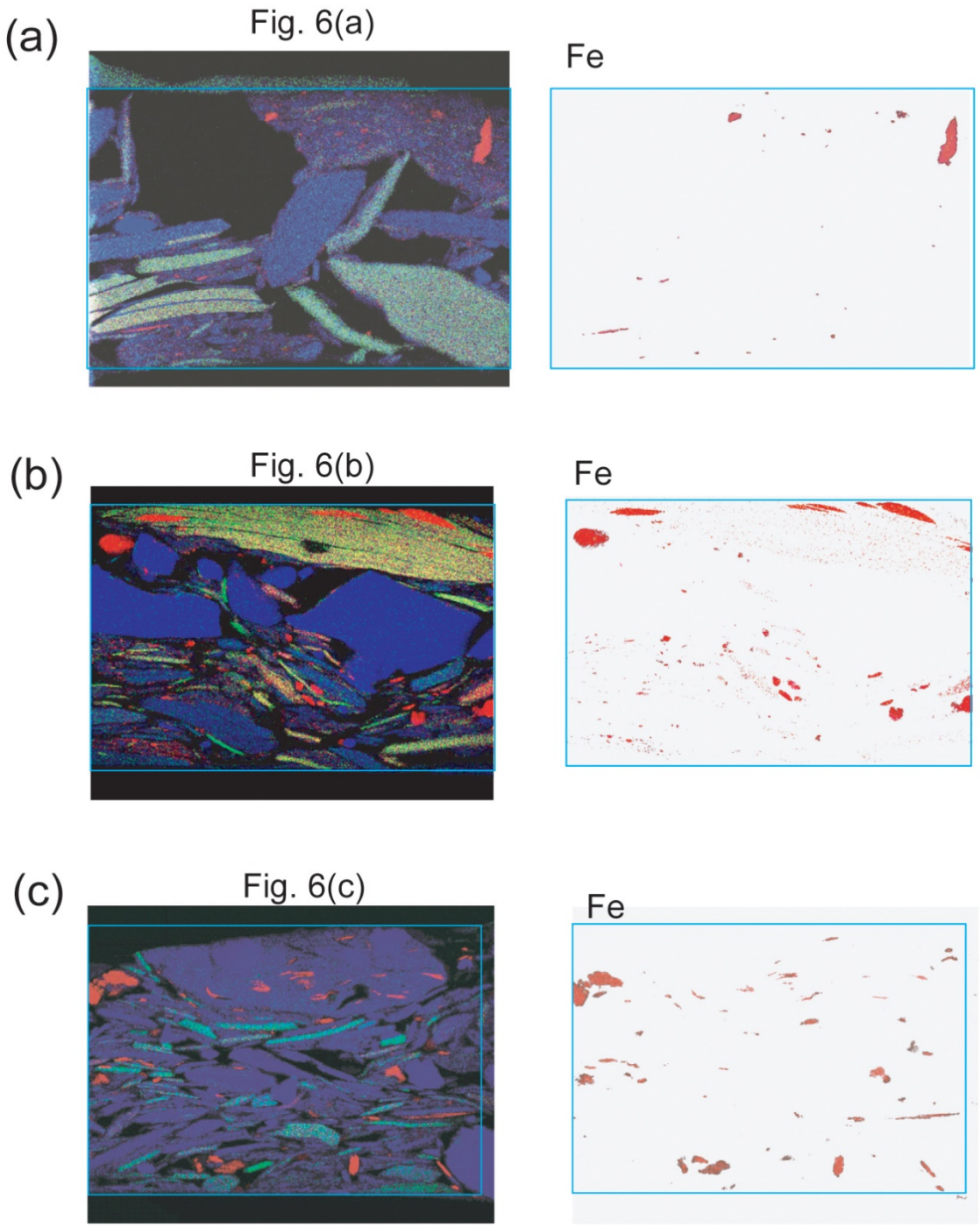

Figure S3. Elemental maps created using TEM images. The total mineral and Fe-rich material maps for the (a) loess fraction in Figure 6a (see main text), (b) paleosol fraction in Figure 6b, and (c) paleosol fraction in Figure 6c. Digital image processing of Fe-rich areas extracted from the elemental maps, and the proportions of Fe-rich areas to total mineral area are: (a) 1.4%, (b) 7.7%, and (c) 4.6%.

Table S1. Results of IRM component analyses.

Sample ID	Compo-nent	Bulk				D1				D2				D3			
		$logB_{1/2}$	DP	$B_{2/1}$	Relative contri.	$logB_{1/2}$	DP	$B_{2/1}$	Relative contri.	$logB_{1/2}$	DP	$B_{2/1}$	Relative contri.	$logB_{1/2}$	DP	$B_{2/1}$	Relative contri.
		(mT)			(%)	(mT)			(%)	(mT)			(%)	(mT)			(%)
LL8 (loess)	1	1.46	0.26	29	20.4	1.46	0.27	29	19.9	1.49	0.29	31	23.1	1.51	0.23	32	55.6
	2	1.99	0.22	97	46.4	1.98	0.29	96	50.9	2.04	0.23	111	45.2	-	-	-	-
	3	2.35	0.82	223	33.2	2.35	1.05	222	29.2	2.34	0.83	220	31.8	2.34	1.04	221	44.4
LS8 (paleosol)	1	1.42	0.32	26	65.3	1.46	0.30	29	30.1	1.44	0.29	28	58.8	1.37	0.27	23	92.5
	2	2.01	0.31	101	24.0	1.85	0.38	72	48.2	2.08	0.38	121	24.1	-	-	-	-
	3	2.35	0.69	222	10.6	2.34	0.83	219	21.7	2.35	1.09	222	17.2	2.34	0.48	220	7.5
XL8 (loess)	1	1.49	0.24	31	13.5	1.36	0.21	23	8.4	1.51	0.21	32	14.5	1.44	0.21	28	65.7
	2	1.94	0.24	88	59.2	1.92	0.28	83	75.0	1.99	0.23	98	67.7	-	-	-	-
	3	2.35	1.12	223	27.3	2.40	1.25	252	16.7	2.26	1.25	183	17.8	2.22	1.25	167	34.3
XS8 (paleosol)	1	1.24	0.26	17	45.2	1.38	0.26	24	17.0	1.49	0.33	31	69.2	1.42	0.24	26	76.2
	2	1.70	0.27	50	37.4	1.87	0.29	75	60.5	-	-	-	-	-	-	-	-
	3	2.23	1.16	171	17.3	2.79	1.16	612	22.6	2.59	1.22	391	30.4	2.59	1.22	391	23.8
LL33 (loess)	1	1.45	0.26	28	17.7	1.50	0.37	32	17.5	1.49	0.27	31	21.8	1.45	0.23	28	70.2
	2	1.92	0.31	82	39.1	1.92	0.31	83	46.5	1.91	0.29	82	38.3	-	-	-	-
	3	2.57	1.08	369	43.2	2.56	1.10	364	36.0	2.55	1.02	358	39.9	2.57	0.94	370	29.8
LS32 (paleosol)	1	1.40	0.28	25	64.6	1.40	0.34	25	54.5	1.39	0.28	25	73.2	1.36	0.30	23	88.7
	2	1.90	0.41	80	19.2	1.88	0.36	76	28.1	1.90	0.39	80	13.5	-	-	-	-
	3	2.57	1.25	371	16.2	2.57	0.75	371	17.4	2.57	1.05	371	13.3	2.56	0.66	364	11.3

$B_{1/2}$: The field at which half of the saturation IRM is reached, DP: one standard deviation of the logarithmic distribution (Heslop *et al*., 2002)

LL8: Lingtai L8, LS8: Lingtai S8, XL8: Xifeng L8, XS8: Xifeng S8, LL33: Lingtai L33, LS32: Lingtai S32